ESTIMATION OF WEAR IN DRY FRICTION DAMPERS AND ITS
EFFECT ON VIBRATION REDUCTION

A THESIS SUBMITTED TO
THE GRADUATE SCHOOL OF NATURAL AND APPLIED SCIENCES
OF
MIDDLE EAST TECHNICAL UNIVERSITY

BY

AYKUT ÇARDAK

IN PARTIAL FULFILLMENT OF THE REQUIREMENTS
FOR
THE DEGREE OF MASTER OF SCIENCE
IN
MECHANICAL ENGINEERING

AUGUST 2022

Approval of the thesis:

ESTIMATION OF WEAR IN DRY FRICTION DAMPERS AND ITS EFFECT ON VIBRATION REDUCTION

submitted by **AYKUT ÇARDAK** in partial fulfillment of the requirements for the degree of **Master of Science** in **Mechanical Engineering, Middle East Technical University** by,

Prof. Dr. Halil Kalıpçılar
Dean, Graduate School of **Natural and Applied Sciences** _____

Prof. Dr. Sahir Arıkan
Head of the Department, **Mechanical Engineering** _____

Prof. Dr. Ender Ciğeroğlu
Supervisor, **Mechanical Engineering, METU** _____

Examining Committee Members:

Prof. Dr. Yiğit Yazıcıoğlu
Mechanical Engineering, METU _____

Prof. Dr. Ender Ciğeroğlu
Mechanical Engineering, METU _____

Assoc. Prof. Dr. Mehmet Bülent Özer
Mechanical Engineering, METU _____

Assist. Prof. Dr. Orkun Özşahin
Mechanical Engineering, METU _____

Assist. Prof. Dr. Mohammad Rahmanian
Aeronautical Engineering, Gebze Technical University _____

Date: 31.08.2022

I hereby declare that all information in this document has been obtained and presented in accordance with academic rules and ethical conduct. I also declare that, as required by these rules and conduct, I have fully cited and referenced all material and results that are not original to this work.

Name Last name : Aykut Çardak

Signature :

ABSTRACT

ESTIMATION OF WEAR IN DRY FRICTION DAMPERS AND ITS EFFECT ON VIBRATION REDUCTION

Çardak, Aykut
Master of Science, Mechanical Engineering
Supervisor: Prof. Dr. Ender Ciğeroğlu

August 2022, 69 pages

Although friction is mostly considered an undesirable phenomenon due to its energy dissipation characteristic, specially designed dry friction dampers utilize this feature to reduce the dynamic response of the system at the resonant frequencies. However, fretting wear due to dry friction during the operational life of the structure may drastically shift the performance from the initial design point and eventually cause drastic failures. Hence, it is important to establish a sophisticated algorithm that couples nonlinear dynamic response solver of frictionally constraint problems with a fretting wear model. In this thesis, the proposed methodology is utilized to find the evolution of dynamic response and surface topography of two widely used case studies which are shrouded blade and grounded blade platforms under ongoing vibration cycles.

Keywords: Nonlinear Vibration, Harmonic Balance Method, Dry Friction Damping, Fretting Wear

ÖZ

KURU SÜRTÜNMELİ SÖNÜMLEYİCİLERDEKİ AŞINMANIN ÖNGÖRÜLMESİ VE BUNUN TİTREŞİM AZLTIMINA ETKİLERİ

Çardak, Aykut
Yüksek Lisans, Makina Mühendisliği
Tez Yöneticisi: Prof. Dr. Ender Ciğeroğlu

Ağustos 2022, 69 sayfa

Sürtünme, sistemin enerjisini sönümleme özelliğinden dolayı çoğunlukla istenmeyen bir fenomen olarak görülse de, özel olarak tasarlanmış kuru sürtünmeli sönümleyiciler, sistemin rezonans frekanslarında dinamik tepkisini azaltmak için bu özelliği kullanır. Bununla birlikte, yapının operasyonel ömrü boyunca kuru sürtünmeden kaynaklanan titreşimsel aşınması, performansı ilk tasarım noktasından büyük ölçüde kaydırabilir ve sonunda ciddi sonuçlara neden olabilir. Bu nedenle, kuru sürtünmeli problemlerinin doğrusal olmayan dinamik tepki çözücüsünü bir sürtünme aşınma modeliyle birleştiren gelişmiş bir algoritma kurmak önemlidir. Bu tezde, tasvir edilen metodoloji kullanılarak, üzerinde sıklıkla çalışılan "shrouded blade" ve "grounded blade platform" örnekleri üzerinden, devamlı titreşim döngüsü altında, dinamik tepki ve yüzey topografisinin değişimi incelenmiştir.

Anahtar Kelimeler: Doğrusal Olmayan Titreşim, Harmonic Balance Method, Kuru Sürtünmeli Sönümleme, Titreşimli Aşınma

To my mother

ACKNOWLEDGMENTS

TABLE OF CONTENTS

LIST OF TABLES

LIST OF FIGURES

FIGURES

LIST OF ABBREVIATIONS

ABBREVIATIONS

HCF	High Cycle Fatigue
HBM	Harmonic Balance Method
DFM	Describing Function Method
RM	Receptance Method
AFT	Alternating Frequency Time
EOM	Equation of Motion
DOF	Degree of Freedom
FRF	Frequency Response Function
FFT	Fast Fourier Transform
FEM	Finite Element Method
CAD	Computer Aided Drawing

CHAPTER 1

INTRODUCTION

1.1   Literature Survey

In mechanical structures, friction is a commonly occurring phenomenon between subcomponents. While these frictional interfaces are undesired most of the time, they are included to the system by the designer on purpose in some engineering fields like turbomachinery. For instance, in gas turbine engines where beam-like blades are exposed to high resonant amplitudes at high speeds, frictional interfaces are intentionally included to prevent high cycle fatigue (HCF) failure and eventually guarantee operational safety and efficiency. The resonant amplitudes are significantly reduced by means of friction which contributes to the overall damping performance of the structure. As a result of this, HCF life can be enhanced, and the maintenance period can be prolonged safely. However, due to the complex nonlinear contact kinematics of the friction phenomenon, building a mathematical model becomes difficult. Hence, modeling the nonlinear behavior of such contact kinematics has drawn great interest such that several friction models have been introduced in the past and summarized by Marques et al. [1]. Among other friction models, Coulomb friction model with discretized Jenkins friction elements [2] has been widely used in this area.

From past to present, several design concepts such as blade-to-ground, blade-to-blade, shroud, and underplatform dampers have been presented by the gas turbine manufacturers which contributed to the development of the friction contact models. Blade-to-ground dampers are the simplest and greatly studied model to damp the blades. For such damper designs, normal load is assumed to be constant while 1D

tangential motion experiences stick and slip phenomena [3]–[7]. Despite the simplicity, the model is quite adequate to predict the forced response of the system. However, for the blade-to-blade, shroud, or underplatform dampers interblade phase angle needs to be considered which brings complexity to the analysis. For such complex systems, elliptical trajectory is followed by the contact point and thus, more sophisticated 2D model was developed [8]–[10]. Although constant normal load assumption simplifies the problem, it cannot always represent the real system where possible normal motion causes normal load variation which may cause separation state along with stick and slip states. Menq et al. [11] first developed variable normal load model with 1D linear motion for single harmonic assumption case. This work is later extended [12] for 3D contact kinematics with variable normal load. Finding the transition angles of stick, slip, and separation states is another important issue that is worked to enhance the accuracy and solution time for single harmonic motion so that transition angles can be found analytically [13].

Although for many nonlinearities and Coulomb friction nonlinearity with single harmonic solution case, transition angles can be derived analytically, Alternating Frequency Time (AFT) Method [14] has been developed to calculate transition angles numerically where it may not be possible to find them numerically. Thus, in the literature, vibrational analyses of dry friction dampers are widely coupled with AFT method [15]–[19]. Firrone et al. [20] also summarized the different types of friction models coupled with AFT method by several case studies.

As mentioned previously, frictionally constrained structures mostly suffer from high cycle failures which may be millions of cycles. More precisely, high frictional loads in a cyclic manner promote fretting wear which causes material removal from contacting surfaces, and thus, this may alter the dynamic response of the system. In order to predict the wear rate, hundreds of formulations have been introduced in the literature by utilizing the methods of solid mechanics and/or empirical relations that were investigated by Meng et al. [21] and Montgomery et al. [22]. Although no agreement has been achieved by the researchers yet, these formulations boil down to a couple of models/approaches like Archard's model [23], wear-energy approach

2

[24]–[26], atomic scale approach [27], and thermodynamics approach [28]. Although thermodynamics and atomic scale approaches give more sophisticated perspective to the problem, either the modeling complexities like large number of unknowns and parameters and yet scarce experimental data make them difficult to apply to real engineering problems when compared with the rest. In the literature, Archard's wear model which mainly contains normal load, material hardness, sliding distance, and experimental wear constant is mostly used to predict wear volume of the contact surface for fretting wear and implemented in the nonlinear dynamics problem first by Laxalde et al. [29] and Salles et al. [30]. In recent years, due to some drawbacks [24] of Archard's model and good correlation of the wear-energy approach with experimental studies [25], [26], nonlinear dynamics problems are coupled with the wear-energy approach [31]–[34] in which dissipated energy over the fretting cycle is directly related with the wear volume by an experimentally determined coefficient.

1.2   Objective of the Thesis

In this thesis, the evolution of contact geometry of dry friction dampers exposed to fretting wear and change in the dynamic response of the structure over the ongoing wear process is investigated. To achieve this goal, analysis is conducted with different algorithms from different perspectives. Moreover, employed methods and algorithms are elaborately developed to reduce the computational expense of the analysis. Lastly, the built-up mathematical model and fretting wear algorithm are verified with numerical case studies.

1.3   Outline of the Thesis

In Chapter 2, the equation of motion nonlinear systems and the frequency domain solution of the system are discussed. As a frequency domain method, Harmonic Balance Method (HBM) is employed to transform a set of nonlinear differential

equations into algebraic equations which are then solved by Newton's method with the Arclength continuation method. To decrease the computational effort, Receptance Method (RM) formulation is also explained in detail.

In Chapter 3, two different macroslip contact models which are 1D dry friction element with normal load variation and 3D dry friction element are presented. Algorithms of these two contact models are deeply discussed with Alternating Frequency Time (AFT) method which is utilized to find the Fourier coefficients of nonlinear internal forcing throughout the thesis. In addition, three different commonly used fretting wear models are covered and compared.

In Chapter 4, by referencing the methodology provided in previous sections, contact and fretting wear models are coupled with each other. Algorithms are built based on wear depth and wear cycle perspectives which are discussed in the upcoming chapter.

In Chapter 5, two case studies, shrouded blade and grounded blade platform are deeply studied to validate the proposed methods and algorithms. Wear topographies and change in dynamic response during the ongoing fretting process are analyzed.

In Chapter 6, thesis is concluded by the discussion of the findings in this work along with recommendations for future studies.

CHAPTER 2

DYNAMIC RESPONSE ANALYSIS OF NONLINEAR SYSTEMS

2.1 Equation of Motion of Nonlinear Systems

Equation of motion (EOM) of general frictionally constraint vibratory system can be expressed in matrix form by neglecting gyroscopic effects as,

$$\mathbf{M\ddot{x}} + i\mathbf{Hx} + \mathbf{Kx} + \mathbf{f_N} = \mathbf{f}, \tag{2.1}$$

where $\mathbf{x}$ is the displacement vector, $\mathbf{M}$, $\mathbf{H}$ and $\mathbf{K}$ are the mass, structural damping, and stiffness matrices, respectively. $\mathbf{f_N}$ is the nonlinear forcing vector due to friction contact and $\mathbf{f}$ is the external excitation forcing vector. i denotes the unit imaginary number. What causes nonlinearity in (2.1) is the nonlinear forcing vector, $\mathbf{f_N}$ which is a function of nonlinear degrees of freedoms (DOFs) of displacement vector, $\mathbf{x}$.

For the solution of (2.1), there are three main approaches used in the literature, analytical, time domain, and frequency domain methods. If the steady state response of the nonlinear problem is a major concern, frequency domain methods are preferred to other methods due to their superior speed.

For the harmonic excitation forcing, solution can also be expressed with harmonics.

$$\mathbf{f} = \sum_{m=0}^{N_h} \mathbf{f}_m e^{im\omega t}, \tag{2.2}$$

$$\mathbf{x} = \sum_{m=0}^{N_h} \mathbf{x}_m e^{im\omega t}, \tag{2.3}$$

where N_h is the number of harmonics included in the solution, $\mathbf{f}_m$ and $\mathbf{x}_m$ are the external forcing and displacement vectors for the mth harmonic in complex form respectively. Similarly, nonlinear forcing can also be described with complex valued summation formula.

$$\mathbf{f_N} = \sum_{m=0}^{N_h} \mathbf{f_N}_m e^{im\omega t}. \tag{2.4}$$

Inserting (2.2), (2.3) and (2.4) to the (2.1) by differentiating (2.3), following nonlinear complex nonlinear algebraic equation can be obtained for each harmonic.

$$\left(\mathbf{K} - (m\omega)^2 \mathbf{M} + i\mathbf{H}\right)\mathbf{x}_m + \mathbf{f_N}_m = \mathbf{f}_m. \tag{2.5}$$

2.2 Harmonic Balance Method (HBM)

Frequency domain methods -such as Harmonic Balance Method (HBM), and Describing Function Method (DFM)- become prominent over the computationally demanding time domain methods. In HBM, both linear and nonlinear part of the problem is expressed with harmonic series and like terms are balanced which results in a set of nonlinear algebraic equations. Assuming harmonic response and including bias term, solution can be written as a real valued harmonic expression.

$$\mathbf{x} = \mathbf{x}_0 + \sum_{m=1}^{N_h} \left(\mathbf{x}_{s_m} \sin(m\theta) + \mathbf{x}_{c_m} \cos(m\theta)\right), \tag{2.6}$$

$$\mathbf{f} = \mathbf{f}_0 + \sum_{m=1}^{N_h} \left(\mathbf{f}_{s_m} \sin(m\theta) + \mathbf{f}_{c_m} \cos(m\theta)\right), \tag{2.7}$$

where $\theta = \omega t$ for convenience, N_h is the total harmonics used in the solution, subscripts s_m, c_m, 0 are representing the sine and cosine coefficients of the mth harmonic and bias term respectively. Similarly, nonlinear forcing vector can also be expressed with sine and cosine form by Fourier expansion.

$$\mathbf{f_N} = \mathbf{f_{N_0}} + \sum_{m=1}^{n} \left(\mathbf{f_{N_{s\,m}}} \sin(m\theta) + \mathbf{f_{N_{c\,m}}} \cos(m\theta) \right). \tag{2.8}$$

Fourier coefficients of (2.8) can be found by Fourier integration as follows,

$$\mathbf{f_{N_{s\,m}}} = \frac{1}{\pi} \int_0^{2\pi} \mathbf{f_N} \sin(m\theta) d\theta, \tag{2.9}$$

$$\mathbf{f_{N_{c\,m}}} = \frac{1}{\pi} \int_0^{2\pi} \mathbf{f_N} \cos(m\theta) d\theta, \tag{2.10}$$

$$\mathbf{f_{N_0}} = \frac{1}{2\pi} \int_0^{2\pi} \mathbf{f_N} d\theta. \tag{2.11}$$

Substituting (2.6), (2.7) and (2.8) into the (2.5) by using Euler's formula, balancing like terms and considering only real valued coefficients, the equation of motion can be expressed in matrix form as follows,

$$\begin{bmatrix} \mathbf{K} & 0 & 0 & 0 \\ 0 & \begin{array}{c|c} \mathbf{K} - \omega^2 \mathbf{M} & -\gamma_1 \mathbf{K} \\ \hline \gamma_1 \mathbf{K} & \mathbf{K} - \omega^2 \mathbf{M} \end{array} & 0 & 0 \\ 0 & 0 & \ddots & 0 \\ 0 & 0 & 0 & \begin{array}{c|c} \mathbf{K} - (m\omega)^2 \mathbf{M} & -\gamma_m \mathbf{K} \\ \hline \gamma_m \mathbf{K} & \mathbf{K} - (m\omega)^2 \mathbf{M} \end{array} \end{bmatrix} \begin{bmatrix} \mathbf{x}_0 \\ \mathbf{x}_{s_1} \\ \mathbf{x}_{c_1} \\ \vdots \\ \mathbf{x}_{s_m} \\ \mathbf{x}_{c_m} \end{bmatrix} \cdots$$

$$+ \begin{bmatrix} \mathbf{f_{N_0}} \\ \mathbf{f_{N_{s\,1}}} \\ \mathbf{f_{N_{c\,1}}} \\ \vdots \\ \mathbf{f_{N_{s\,m}}} \\ \mathbf{f_{N_{c\,m}}} \end{bmatrix} - \begin{bmatrix} \mathbf{f}_0 \\ \mathbf{f}_{s\,1} \\ \mathbf{f}_{c\,1} \\ \vdots \\ \mathbf{f}_{s\,m} \\ \mathbf{f}_{c\,m} \end{bmatrix} = \mathbf{0}. \tag{2.12}$$

where γ_m is the structural damping coefficient of mth harmonic for proportional damping. Structural damping is calculated by multiplication of structural damping coefficient and stiffness matrix. However, for real engineering problems, systems

have large number of DOFS which results in a large number of unknowns in (2.12). To overcome this difficulty, Receptance Method (RM) is employed in this thesis.

2.3   Receptance Method (RM)

Receptance method decreases the number of nonlinear algebraic equations if the number of nonlinear DOFs is much less than the total number of DOFs. In RM, unknowns in the displacement vector are split into its linear and nonlinear DOFs and system matrices in (2.5) is reordered accordingly. Complex valued equation of motion can be written for m^{th} harmonic as follows,

$$\left[\mathbf{K} - (m\omega)^2 \mathbf{M} + i\mathbf{H} \right] \begin{bmatrix} \mathbf{x}_{l\,m} \\ \mathbf{x}_{n\,m} \end{bmatrix} + \begin{bmatrix} 0 \\ \mathbf{f}_{\mathbf{N}\,m} \end{bmatrix} = \begin{bmatrix} \mathbf{f}_{l\,m} \\ \mathbf{f}_{n\,m} \end{bmatrix}. \tag{2.13}$$

where subscript $\mathbf{x}_l$ denotes linear DOFs while $\mathbf{x}_n$ denotes the nonlinear DOFs. Receptance matrix of the linear system for the mth harmonic can be expressed as follows,

$$\mathbf{A} = \left(\mathbf{K} - (m\omega)^2 \mathbf{M} + i\mathbf{H} \right)^{-1}. \tag{2.14}$$

Multiplying both sides of (2.13) by the inverse of the receptance matrix, the following complex nonlinear algebraic equation is obtained.

$$\begin{bmatrix} \mathbf{x}_{l\,m} \\ \mathbf{x}_{n\,m} \end{bmatrix} + \begin{bmatrix} \mathbf{A}_{ll\,m} & \mathbf{A}_{ln\,m} \\ \mathbf{A}_{nl\,m} & \mathbf{A}_{nn\,m} \end{bmatrix} \begin{bmatrix} \mathbf{0} \\ \mathbf{f}_{\mathbf{N}\,m} \end{bmatrix} - \begin{bmatrix} \mathbf{A}_{ll\,m} & \mathbf{A}_{ln\,m} \\ \mathbf{A}_{nl\,m} & \mathbf{A}_{nn\,m} \end{bmatrix} \begin{bmatrix} \mathbf{f}_{l\,m} \\ \mathbf{f}_{n\,m} \end{bmatrix} = \mathbf{0}. \tag{2.15}$$

Since the nonlinear forces depend on $\mathbf{x}_n$, only the second row of (2.15) should be solved iteratively. Hence, the nonlinear algebraic equation to be solved is expressed as follows,

$$\mathbf{x}_{n\,m} + \mathbf{A}_{nn\,m} \mathbf{f}_{\mathbf{N}\,m} - \begin{bmatrix} \mathbf{A}_{nl\,m} & \mathbf{A}_{nn\,m} \end{bmatrix} \begin{bmatrix} \mathbf{f}_{l\,m} \\ \mathbf{f}_{n\,m} \end{bmatrix} = \mathbf{0}. \tag{2.16}$$

As illustrated in (2.12), complex nonlinear equations in (2.16) should be represented in real valued matrix form. Note that, while transforming equations from complex to the real form, real and imaginary terms become the coefficients of cosine and sine terms, respectively. Assuming harmonic solution by including bias terms as discussed in Section 2.2,

$$
\mathbf{r}\left(\mathbf{x}_n,\omega,m\right) =
\begin{bmatrix}
\mathbf{x}_{n_0} \\
\mathbf{x}_{n_{s\,1}} \\
\mathbf{x}_{n_{c\,1}} \\
\vdots \\
\mathbf{x}_{n_{s\,m}} \\
\mathbf{x}_{n_{c\,m}}
\end{bmatrix}
+
\begin{bmatrix}
\mathbf{A}_{nn_0} & 0 & 0 & 0 \\
0 & \mathbf{\Theta}_1(1) & 0 & 0 \\
0 & 0 & \ddots & 0 \\
0 & 0 & 0 & \mathbf{\Theta}_1(m)
\end{bmatrix}
\cdot
\begin{bmatrix}
\mathbf{f}_{n_0} \\
\mathbf{f}_{n_{s\,1}} \\
\mathbf{f}_{n_{c\,1}} \\
\vdots \\
\mathbf{f}_{n_{s\,m}} \\
\mathbf{f}_{n_{c\,m}}
\end{bmatrix}
+
$$

$$
\begin{bmatrix}
\mathbf{A}_{nl_0} & \mathbf{A}_{nn_0} & 0 & 0 & 0 \\
0 & \mathbf{\Theta}_2(1) & 0 & 0 \\
0 & 0 & \ddots & 0 \\
0 & 0 & 0 & \mathbf{\Theta}_2(m)
\end{bmatrix}
\cdot \mathbf{f} = 0.
$$

$$(2.17)$$

where $\mathbf{A}_0$ can be calculated by taking $\omega = 0$ in (2.14) and $\mathbf{\Theta}_1$, $\mathbf{\Theta}_2$ and $\mathbf{f}$ denotes the following expressions,

$$
\mathbf{\Theta}_1(m) =
\begin{bmatrix}
\mathrm{Re}\left(\mathbf{A}_{nn_m}\right) & -\mathrm{Im}\left(\mathbf{A}_{nn_m}\right) \\
\mathrm{Im}\left(\mathbf{A}_{nn_m}\right) & \mathrm{Re}\left(\mathbf{A}_{nn_m}\right)
\end{bmatrix},
\qquad (2.18)
$$

$$
\mathbf{\Theta}_2(m) =
\begin{bmatrix}
\mathrm{Re}\left(\mathbf{A}_{nl_m}\right) & -\mathrm{Im}\left(\mathbf{A}_{nl_m}\right) & \mathrm{Re}\left(\mathbf{A}_{nn_m}\right) & -\mathrm{Im}\left(\mathbf{A}_{nn_m}\right) \\
\mathrm{Im}\left(\mathbf{A}_{nl_m}\right) & \mathrm{Re}\left(\mathbf{A}_{nl_m}\right) & \mathrm{Im}\left(\mathbf{A}_{nn_m}\right) & \mathrm{Re}\left(\mathbf{A}_{nn_m}\right)
\end{bmatrix},
\quad (2.19)
$$

$$
\mathbf{f} =
\begin{bmatrix}
\mathbf{f}_{l_0}{}^{\mathbf{T}} & \mathbf{f}_{n_0}{}^{\mathbf{T}} & \mathbf{f}_{l_{s\,1}}{}^{\mathbf{T}} & \mathbf{f}_{n_{s\,1}}{}^{\mathbf{T}} & \mathbf{f}_{l_{c\,1}}{}^{\mathbf{T}} & \mathbf{f}_{n_{c\,1}}{}^{\mathbf{T}} & \cdots & \mathbf{f}_{l_{s\,m}}{}^{\mathbf{T}} & \mathbf{f}_{n_{s\,m}}{}^{\mathbf{T}} & \mathbf{f}_{l_{c\,m}}{}^{\mathbf{T}} & \mathbf{f}_{n_{c\,m}}{}^{\mathbf{T}}
\end{bmatrix}^{\mathbf{T}}.
$$

$$(2.20)$$

9

$\mathbf{r}(\mathbf{x}_n, \omega, m)$ is called residual vector that needs to be solved numerically as illustrated in 2.4. After solving the nonlinear part of the problem, the linear part of the mth harmonic can be solved analytically from the first row of (2.15).

$$x_{l_m} + \mathbf{A}_{ln_m} \mathbf{f}_{\mathbf{N}_m} - \begin{bmatrix} \mathbf{A}_{ll_m} & \mathbf{A}_{ln_m} \end{bmatrix} \begin{bmatrix} \mathbf{f}_{l_m} \\ \mathbf{f}_{n_m} \end{bmatrix} = \mathbf{0}. \tag{2.21}$$

Let N is the total number of DOFs, N_n is the total number of nonlinear DOFs, and $m = 1, 2, \ldots, N_h$. Since only nonlinear DOFs are considered in (2.17), computational cost of numerical calculation is reduced from $(2N_h + 1).N$ to $(2N_h + 1).N_n$ when N_n is considerably less than N. It should also be noted that, for large number of N, especially when finite element method is utilized, it would be advantageous to get receptance matrix by modal analysis method, rather than inverting of dynamic stiffness matrix in (2.14).

$$\mathbf{A}(\omega) = \sum_{r=1}^{N_m} \frac{\boldsymbol{\varphi}_r \cdot \boldsymbol{\varphi}_r^{\mathbf{T}}}{(1 + i\gamma_r).\omega_r^2 - (m\omega)^2}, \tag{2.22}$$

where N_m is the number of modes extracted from the model, $\boldsymbol{\varphi}_r$, γ_r and ω_r are the mass normalized mode shape, loss factor for proportional damping, and undamped natural frequency of the rth mode. Note that mode shapes are extracted from the finite element software program. In this study, ANSYS Workbench is utilized for this purpose.

2.4   Newton's Method with Arclength Continuation

To solve the residual vector, $\mathbf{r}(\mathbf{x}_n, \omega, m)$, indicated in (2.17), employing a numerical method is necessary since the nonlinear force vector is a function of the displacement vector, $\mathbf{x}_n$, which makes the problem difficult to solve analytically.

By Taylor Series expansion around $\mathbf{x}_n$ and neglecting higher order terms,

$$\mathbf{r}\left(\mathbf{x}_n + \Delta\mathbf{x}_n, \omega, m\right) = \mathbf{r}\left(\mathbf{x}_n, \omega, m\right) + \mathbf{J}\left(\mathbf{x}_n, \omega, m\right).\Delta\mathbf{x}_n. \qquad (2.23)$$

where, $\mathbf{J}$ is the Jacobian matrix. Taking $\mathbf{r}\left(\mathbf{x}_n + \Delta\mathbf{x}_n, \omega, m\right) = \mathbf{0}$ and rewriting (2.23)

$$\mathbf{r}\left(\mathbf{x}_n, \omega, m\right) + \mathbf{J}\left(\mathbf{x}_n, \omega, m\right).\Delta\mathbf{x}_n = \mathbf{0}, \qquad (2.24)$$

$$\Delta\mathbf{x}_n = \mathbf{x}_n^{k+1} - \mathbf{x}_n^k, \qquad (2.25)$$

where subscript k is the already calculated previous iteration while $k+1$ is the new potential solution which is calculated iteratively until reaching the predetermined threshold error value. When (2.25) plugged into (2.24), single iteration of Newton's Method can be written as follows,

$$\mathbf{x}_n^{k+1} = \mathbf{x}_n^k - \mathbf{J}\left(\mathbf{x}_n^k, \omega, m\right)^{-1}.\mathbf{r}\left(\mathbf{x}_n^k, \omega, m\right). \qquad (2.26)$$

Jacobian matrix $\mathbf{J}$ can be calculated by forward difference formula as follows,

$$\mathbf{J}\left(\mathbf{x}_n^k, \omega, m\right) = \frac{\mathbf{r}\left(\mathbf{x}_n^k + h_j.e_j, \omega, m\right) - \mathbf{r}\left(\mathbf{x}_n^k, \omega, m\right)}{h_j}, \qquad (2.27)$$

where, e_j is the unit vector in the jth direction and h_j is a scaled step size used to avoid subtractive cancelation.

In order to obtain Frequency Response Function (FRF) in which frequency response is sought in a specific frequency interval, (2.26) needs to be swept in the desired frequency range. This sweeping procedure is called as path following method. Two of the widely used path following methods are Homotopy continuation and Arclength continuation methods.

In Homotopy continuation, the previous solution is taken as an initial guess, and Newton's method which is formulated in (2.26) is utilized to find a new solution at the corresponding frequency value, ω, that is changed incrementally. If the response

11

sharply changes with changing ω, Newton's method may not be able to converge to the new solution from the previous solution information. In this case, step size of the frequency sweep is needed to be decreased. The downside of Homotopy continuation stands out when the nonlinearity becomes dominant and FRF makes returns between some frequency intervals which causes multiple solutions at these regions.
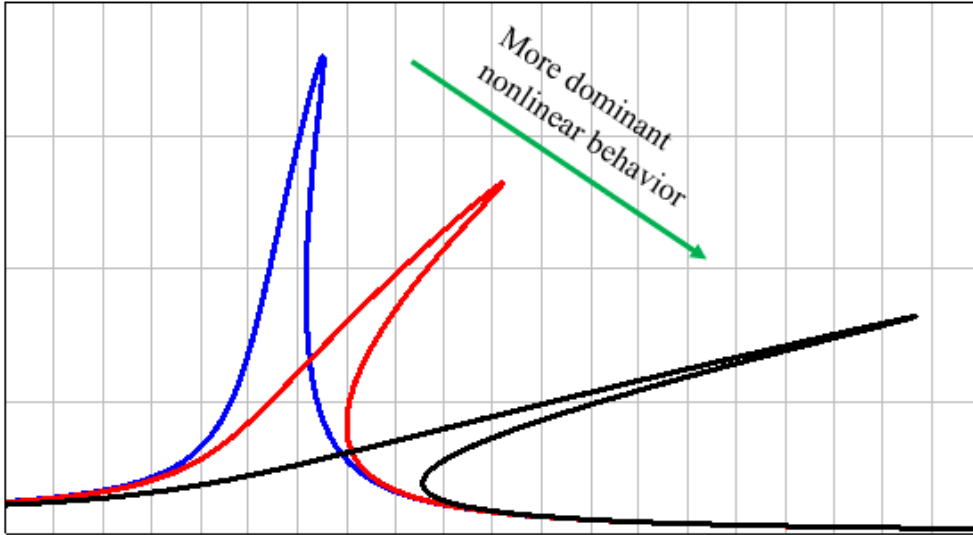
Figure 2.1 FRF for the System with Cubic Stiffness

Figure 2.1 is a simple illustration of nonlinear behavior where steeper turning occurs as the nonlinearity increases. As a result, the Jacobian matrix converges to zero which causes the inverse of the Jacobian matrix singular in (2.26).

Thus, Arclength continuation method [35] is developed to follow the path even if it reverses the direction. Hence, as a continuation parameter, frequency becomes another unknown besides $\mathbf{x}_n$ and unknown vector, $\mathbf{q}$ can be constructed as follows,

$$\mathbf{q} = \begin{bmatrix} \mathbf{x}_n \\ \omega \end{bmatrix}. \tag{2.28}$$

The newly added parameter brings an additional equation that comes from a hypothetical sphere with a radius of Δs and centered at the previous solution point.

$$\left(\mathbf{x}_n^j - \mathbf{x}_n^{j-1}\right)^2 + \left(\omega^j - \omega^{j-1}\right)^2 = \Delta s^2, \tag{2.29}$$

where j denotes the index of the solution point.

Equation of hypothetical sphere can alternatively be written in the following way,

$$h\left(\mathbf{x}_n^j, \omega^j\right) = \Delta\mathbf{q}^{j\,\mathrm{T}} \cdot \Delta\mathbf{q}^j - \Delta s^2 = 0, \tag{2.30}$$

where,

$$\Delta\mathbf{q}^j = \begin{bmatrix} \mathbf{x}_n^j - \mathbf{x}_n^{j-1} \\ \omega^j - \omega^{j-1} \end{bmatrix}. \tag{2.31}$$

Finally, Newton's formulation expressed in (2.26) can be expanded by considering additional unknown and equation,

$$\mathbf{q}^{j+1} = \mathbf{q}^j - \begin{bmatrix} \dfrac{\partial\mathbf{r}\left(\mathbf{x}_n^j, \omega, m\right)}{\partial\mathbf{x}_n^j} & \dfrac{\partial\mathbf{r}\left(\mathbf{x}_n^j, \omega, m\right)}{\partial\omega} \\ \dfrac{\partial h\left(\mathbf{x}_n^j, \omega, m\right)}{\partial\mathbf{x}_n^j} & \dfrac{\partial h\left(\mathbf{x}_n^j, \omega, m\right)}{\partial\omega} \end{bmatrix}^{-1} \begin{bmatrix} \mathbf{r}\left(\mathbf{x}_n^j, \omega, m\right) \\ h\left(\mathbf{x}_n^j, \omega, m\right) \end{bmatrix}, \tag{2.32}$$

where,

$$\begin{bmatrix} \dfrac{\partial h\left(\mathbf{x}_n^j, \omega, m\right)}{\partial\mathbf{x}_n^j} & \dfrac{\partial h\left(\mathbf{x}_n^j, \omega, m\right)}{\partial\omega} \end{bmatrix} = \begin{bmatrix} 2\Delta\mathbf{q}^j \end{bmatrix}^{\mathrm{T}}. \tag{2.33}$$

(2.32) is repeated for a single solution point till the error drops below an error criterion and this procedure is followed for each solution point. Although, convergence and resolution of the solution highly depend on arclength step size value, Δs, small step size brings computational cost to the solver. Thus, Δs parameter should be updated after each solution point. This method is called as an adaptive step size algorithm.

$$\Delta s^{j+1} = \Delta s^j \cdot \left(\frac{\eta_{opt}^{iter}}{\eta_j^{iter}} \right)^{1/3}, \qquad (2.34)$$

where, η_j^{iter} is the total number of iterations reached at the current solution point, j and η_{opt}^{iter} is the optimum iteration number that can be tuned accordingly.

CHAPTER 3

MATHEMATICAL MODELLING OF CONTACT AND FRETTING WEAR

3.1 Contact Modelling

When two bodies are in contact with each other, they induce friction force to each other in opposing directions. There are basically two force components which are tangential and normal. Predicting the contact kinematics and establishing sophisticated models to find force components have become a key issue in the past. Due to the mathematical simplicity, node to node macroslip friction models are widely used where gross slip is assumed at the contact interface. Hence, in this section two widely used macroslip contact models which are 1D dry friction element with normal load variation and 2D dry friction element with normal load variation are discussed and formulated. Both models are derived from the Coulomb friction model by adding extra DOFs and stiffness elements which are detailed in the oncoming subsections.

3.1.1 Alternating Frequency Time (AFT) Method

As discussed in Section 2.2, nonlinear internal forces need to be expressed with harmonic representation in the frequency domain which is formulated from (2.8) to (2.11). However, it may not be possible to handle Fourier integrations neatly when transition angles between states cannot be determined exactly like multi-harmonic solution of the dry friction element with normal load variation. Even if it's possible to calculate the transition angles analytically in some cases, formulation and programming are quite complicated. Thanks to its simplicity and ease of use, the Alternating Frequency Time (AFT) Method is utilized by many researchers. However, it should be noted that AFT brings huge computational cost, inaccuracy,

and even sometimes causes convergence problems to the solver. Hence, these drawbacks should be kept in mind while using AFT.

In the AFT method, displacements are converted from the frequency domain to the time domain by discretization, and nonlinear forces are evaluated in the time domain by obeying Coulomb's friction law. This phase is also called as a time-marching prediction-correction algorithm. After determining the nonlinear forces at each discretized time, Fast Fourier Transform (FFT) is utilized to convert nonlinear forces back to the frequency domain again. The methodology of AFT is illustrated in Figure 3.1.
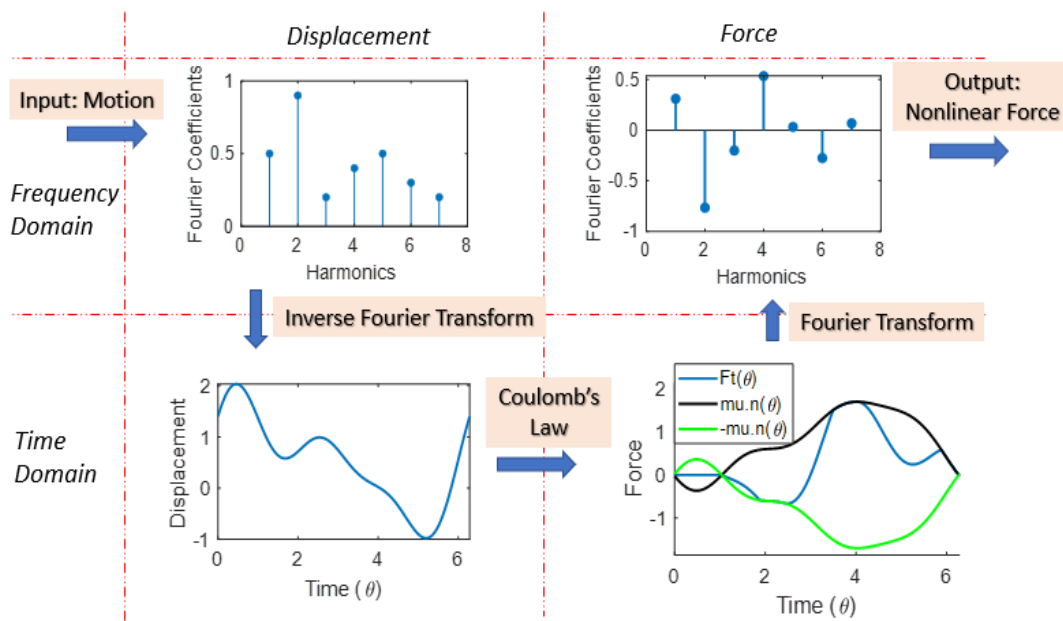

Figure 3.1 Methodology of AFT Algorithm

Thus, this method enables to combine upsides of both frequency and time domain approaches. In this section, the AFT method is utilized in the formulation of both contact models.

3.1.2 1D Dry Friction Element with Normal Load Variation

1D dry friction element with normal load variation induced by normal motion is simple but well enough to model the contacts that occur at shroud-wise interfaces. As shown in Figure 3.2, the relative motion of two contacting bodies is represented with Body 1 while Body 2 is grounded for the sake of simplification. k_u, k_v, μ, $u(\theta)$, $v(\theta)$, $w(\theta)$, n_0 are the tangential contact stiffness, normal contact stiffness, coefficient of friction, tangential relative motion, normal relative motion, slip motion, and preload, respectively. 1D dry friction element with normal load variation can experience stick, slip, and separation conditions.
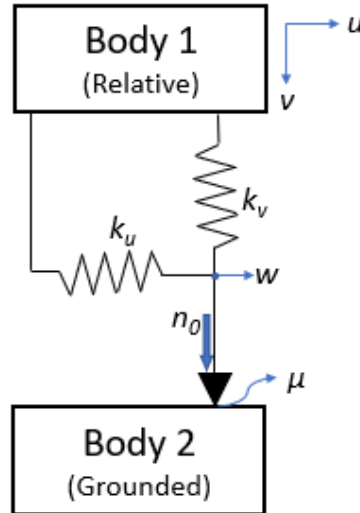
Figure 3.2 1D Dry Friction Model with Normal Load Variation Induced by Normal Motion

To illustrate the pseudo-algorithm of the AFT method used in this contact model, consider instant θ_i where $\theta_i = \omega t_i$. First, check whether there exists separation or not. If the following condition is satisfied, the contact point is at the separation state.

$$n_0 + k_v v(\theta_i) < 0, \tag{3.1}$$

In this case, the nonlinear contact forces are zero, and slip motion is equal to the relative displacement.

17

$$n(\theta_i) = 0, \tag{3.2}$$

$$f_t(\theta_i) = 0, \tag{3.3}$$

$$w(\theta_i) = u(\theta_i), \tag{3.4}$$

where, $n(\theta_i)$ and $f_t(\theta_i)$ are the normal force, tangential friction force in the time domain at the instant of θ_i, respectively. Next, if the condition in (3.1) is not satisfied, i.e. there exists contact between the two bodies, there are two possibilities are remaining: stick or slip. The normal load acting on the contact point can be obtained as follows,

$$n(\theta_i) = n_0 + k_v v(\theta_i). \tag{3.5}$$

Regardless of the actual state, always assume stick state at first and check whether this assumption is correct or not using the following relation,

$$k_u |u(\theta_i) - w(\theta_{i-1})| < \mu n(\theta_i). \tag{3.6}$$

If the condition in (3.6) is satisfied, contact status is in stick state; hence, slip motion is the same as the slip motion at the previous step and the nonlinear tangential friction force can be calculated as follows,

$$w(\theta_i) = w(\theta_{i-1}), \tag{3.7}$$

$$f_t(\theta_i) = k_u \left[u(\theta_i) - w(\theta_i) \right]. \tag{3.8}$$

If (3.6) is not satisfied, contact status at the instant θ_i should be slip. Then, slip motion can be updated as follows,

$$w(\theta_i) = u(\theta_i) - \frac{\mu n(\theta_i)}{k_u}. \tag{3.9}$$

During the slip state, tangential friction force equals to the normal load.

$$f_t(\theta_i) = \mu n(\theta_i) = \mu \left[n_0 + k_v v(\theta_i) \right]. \tag{3.10}$$

This procedure is repeated till steady state is reached. To the author's knowledge, the algorithm of 1D dry friction element with normal load variation converges in two cycles if there is no separation. Note that, if condition in (3.1) is satisfied and it's known that Body 1 experiences separation, repeating the time-marching procedure over one cycle is enough. The reason for this, the calculation of normal force $n(\theta)$ doesn't depend on the prediction-correction algorithm but can be calculated exactly. Hence, the first instant that separation occurs should be the starting instant of single a cycle sweep. As one may guess, the accuracy and convergence of the AFT algorithm highly depend on the step size used during the time-marching procedure.

3.1.2.1 Analytical Jacobian for 1D Dry Friction Element with Normal Load Variation

As indicated in (2.27), Newton's method includes Jacobian matrix for every iterative solution which makes it computationally most expensive function in the solver. There are basically two ways of calculating Jacobian, numerically or analytically. Due to the high computational expense of numerical calculation for especially large number of nonlinear DOFs, analytical Jacobian needs to be implemented to overcome this problem.

As explained in 2.2, solution can be represented with the real valued harmonic solution as expressed in (2.6). Similarly, tangential and normal relative motion can be written as follows,

$$u(\theta_i) = u_0 + \sum_{m=1}^{N_h} \left(u_{s_m} \sin(m\theta) + u_{c_m} \cos(m\theta) \right), \tag{3.11}$$

$$v(\theta_i) = v_0 + \sum_{m=1}^{N_h} \left(v_{s_m} \sin(m\theta) + v_{c_m} \cos(m\theta) \right). \tag{3.12}$$

In this part, formulation is shown for bias term and m^{th} harmonic. According to the harmonic index, formulations can be further extended to each harmonic respectively.

For stick state, tangential force in the dry friction element at the instant θ_i can be written as an alternative form of (3.8) as follows,

$$f_t(\theta_i) = k_u \left[u(\theta_i) - u(\theta_{i-1}) \right] + f_t(\theta_{i-1}).$$

(3.13)

Derivation with respect to u_0, v_0, u_{s_m}, u_{c_m}, v_{s_m} and v_{c_m} for the mth harmonic,

$$\frac{\partial f_t(\theta_i)}{\partial u_0} = \frac{\partial f_t(\theta_{i-1})}{\partial u_0},$$

(3.14)

$$\frac{\partial f_t(\theta_i)}{\partial v_0} = \frac{\partial f_t(\theta_{i-1})}{\partial v_0},$$

(3.15)

$$\frac{\partial f_t(\theta_i)}{\partial u_{s_m}} = k_u \left(\sin(m\theta_i) - \sin(m\theta_{i-1}) \right) + \frac{\partial f_t(\theta_{i-1})}{\partial u_{s_m}},$$

(3.16)

$$\frac{\partial f_t(\theta_i)}{\partial v_{s_m}} = \frac{\partial f_t(\theta_{i-1})}{\partial v_{s_m}},$$

(3.17)

$$\frac{\partial f_t(\theta_i)}{\partial u_{c_m}} = k_u \left(\cos(m\theta_i) - \cos(m\theta_{i-1}) \right) + \frac{\partial f_t(\theta_{i-1})}{\partial u_{c_m}},$$

(3.18)

$$\frac{\partial f_t(\theta_i)}{\partial v_{c_m}} = \frac{\partial f_t(\theta_{i-1})}{\partial v_{c_m}}.$$

(3.19)

For slip state, tangential force at θ_i can be expressed as (3.10) and partial derivation of (3.10) with respect to v_0, v_{s_m} and v_{c_m} reveal the following result,

$$\frac{\partial f_t(\theta_i)}{\partial v_0} = \mu k_v,$$

(3.20)

$$\frac{\partial f_t(\theta_i)}{\partial v_{s_m}} = \mu k_v \sin(m\theta_i), \tag{3.21}$$

$$\frac{\partial f_t(\theta_i)}{\partial v_{c_m}} = \mu k_v \cos(m\theta_i). \tag{3.22}$$

Since (3.10) doesn't include u_0, u_{s_m} and u_{c_m}, partial derivation with respect to these constants are all zero.

$$\frac{\partial f_t(\theta_i)}{\partial u_0} = \frac{\partial f_t(\theta_i)}{\partial u_{s_m}} = \frac{\partial f_t(\theta_i)}{\partial u_{c_m}} = 0. \tag{3.23}$$

As emphasized in the previous part, tangential and normal forces during separation are zero which makes the derivatives of both force components with respect to all coefficients zero for the separation case.

$$\frac{\partial f_t(\theta_i)}{\partial u_0} = \frac{\partial f_t(\theta_i)}{\partial v_0} = \frac{\partial f_t(\theta_i)}{\partial u_{s_m}} = \frac{\partial f_t(\theta_i)}{\partial v_{s_m}} = \frac{\partial f_t(\theta_i)}{\partial u_{c_m}} = \frac{\partial f_t(\theta_i)}{\partial v_{c_m}} = 0, \tag{3.24}$$

$$\frac{\partial n(\theta_i)}{\partial v_0} = \frac{\partial n(\theta_i)}{\partial u_{s_m}} = \frac{\partial n(\theta_i)}{\partial v_{s_m}} = \frac{\partial n(\theta_i)}{\partial u_{c_m}} = \frac{\partial n(\theta_i)}{\partial v_{c_m}} = 0 \tag{3.25}$$

Lastly, partial derivatives of normal force during the stick and slip states need to be analyzed. For both, stick and slip states, normal force is represented with (3.5). Partial derivation with respect to v_0, v_{s_m} and v_{c_m} are result in following expressions,

$$\frac{\partial n(\theta_i)}{\partial v_0} = k_v, \tag{3.26}$$

$$\frac{\partial n(\theta_i)}{\partial v_{s_m}} = k_v \sin(m\theta_i), \tag{3.27}$$

.

$$\frac{\partial n(\theta_i)}{\partial v_{c_m}} = k_v \cos(m\theta_i). \tag{3.28}$$

Since there is no u_0, u_{s_m} and u_{c_m} term included in (3.5), partial derivation with respect to these terms are zero.

$$\frac{\partial n(\theta_i)}{\partial u_0} = \frac{\partial n(\theta_i)}{\partial u_{s_m}} = \frac{\partial n(\theta_i)}{\partial u_{c_m}} = 0 \tag{3.29}$$

Equations from (3.14) to (3.29) are partial derivations of force components with respect to each Fourier coefficients that corresponds to contact indices in the time domain. However, HBM is a frequency domain method, and partial derivatives of Fourier constants of nonlinear force components with respect to displacement vector should be found. Consider the EOM in (2.17) obtained by RM and use this notation for frequency domain nonlinear force Fourier coefficients. Additionally, superscripts $_t$ and $_n$ is added outside of the parenthesis to denote the force components which are tangential and normal directions respectively. To prove the formulation without complicating it, only the bias term of nonlinear force in the tangential direction and sine term of nonlinear force in the normal direction is derivated with respect to v_0 and u_{s_m} respectively.

$$\frac{\partial \left(\mathbf{f}_{n_0} \right)^t}{\partial v_0} = \frac{\partial}{\partial v_0} \left[\frac{1}{2\pi} \int_0^{2\pi} \mathbf{f_t} \, d\theta \right], \tag{3.30}$$

$$\frac{\partial \left(\mathbf{f}_{n_{s\,m}} \right)^n}{\partial u_{s_m}} = \frac{\partial}{\partial u_{s_m}} \left[\frac{1}{\pi} \int_0^{2\pi} \mathbf{n} \sin(\theta) \, d\theta \right]. \tag{3.31}$$

Note that $\mathbf{f_t}$ and $\mathbf{n}$ are the tangential and normal time domain force arrays. Applying Leibniz's rule, partial derivatives can be expressed in alternative form as,

$$\frac{\partial \left(\mathbf{f}_{n\,0} \right)^t}{\partial v_0} = \frac{1}{2\pi} \left[\int_0^{2\pi} \frac{\partial \mathbf{f_t}}{\partial v_0} d\theta \right], \tag{3.32}$$

$$\frac{\partial \left(\mathbf{f}_{n\,s\,m} \right)^n}{\partial u_{s\,m}} = \frac{1}{\pi} \left[\int_0^{2\pi} \frac{\partial \mathbf{n}}{\partial u_{s\,m}} \sin(\theta) d\theta \right]. \tag{3.33}$$

If N_h harmonics are included to the solution, considering force and displacement terms in tangential and normal directions, there exist $2 \times (2N_h + 1)$ variables for a single dry friction element. Thus, to build the Jacobian matrix due to the nonlinear force, $\left[2 \times (2N_h + 1) \right]^2$ integral calculations are needed as two of them are exemplified in (3.32) and (3.33).

Thus, this method enables to obtain Jacobian which is formulated in (2.27) an alternative way and when the RM is used, it can be written as follows,

$$\mathbf{J}\left(\mathbf{x}_n^k, w, m \right) = \mathbf{I} + \begin{bmatrix} \mathbf{A}_{nn\,0} & 0 & 0 & 0 \\ 0 & \mathbf{\Theta_1}(1) & 0 & 0 \\ 0 & 0 & \ddots & 0 \\ 0 & 0 & 0 & \mathbf{\Theta_1}(m) \end{bmatrix} . \mathbf{J_n}\left(\mathbf{x}_n^k, m \right), \tag{3.34}$$

where, $\mathbf{J_n}$ and $\mathbf{I}$ are the Jacobian of the nonlinear force vector and identity matrix, respectively. As one may easily deduce that (2.27) has a residual vector, $\mathbf{r}\left(\mathbf{x}_n, \omega, m \right)$, in the formulation which is called as many as the square of the number of nonlinear DOFs while (3.34) calls the residual vector only once during the calculation of $\mathbf{J_n}\left(\mathbf{x}_n^k, m \right)$. That's the reason why analytical Jacobian is computationally advantageous over numerical calculation.

3.1.3   3D Dry Friction Element

In some engineering problems like dynamic characteristics of a wedge damper, the contact plane makes 2D motion and the previous contact model becomes insufficient. To better understand and model the contact kinematics, 3D dry friction is introduced in this chapter. Similar to the previous 1D model, Body 1 represents the relative motion between connected nonlinear DOFs at the contact plane whilst Body 2 is grounded. As shown in Figure 3.3, contact parameters $\mathbf{K_t}$, k_v, $u(\theta)$, $v(\theta)$, $w(\theta)$, μ and n_0 are denoted for 2×2 tangential contact stiffness matrix, normal contact stiffness, tangential relative motion, normal relative motion, slip motion, coefficient of friction, and preload, respectively. Note that directions of u and w are arbitrarily drawn, thus both have components in x and y directions which are local coordinates describing tangential contact plane.
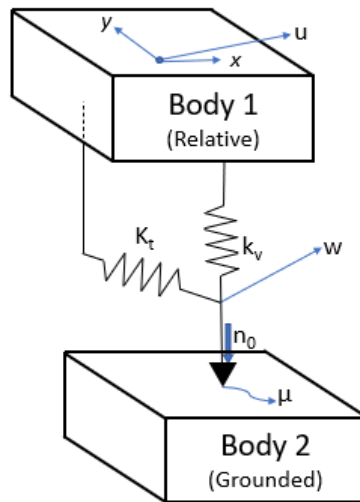

Figure 3.3 3D Dry Friction Model

Due to the manufacturing deficiencies and different surface finishes between contact interfaces, tangential contact stiffness matrix should be considered anisotropic. For the case where $k_{xy} = k_{yx} = 0$, tangential contact would be isotropic, and this model would be equivalent to two 1D dry friction elements connected in both x and y directions separately.

24

$$\mathbf{K_t} = \begin{bmatrix} k_{xx} & k_{xy} \\ k_{yx} & k_{yy} \end{bmatrix}, \tag{3.35}$$

The working algorithm of this dry friction model is similar to the previous one with slight formulation differences. Whether separation exists over a single vibration cycle or not is checked at first by (3.1). If this condition is satisfied, normal contact force is zero as indicated in (3.2). Besides this, tangential contact forces are zero, and slip motions are equal to relative displacements in both directions at the instant θ_i as shown below.

$$f_{t_x}(\theta_i) = f_{t_y}(\theta_i) = 0, \tag{3.36}$$

$$w_x(\theta_i) = u_x(\theta_i), \tag{3.37}$$

$$w_y(\theta_i) = u_y(\theta_i). \tag{3.38}$$

where subscripts $_x$ and $_y$ are representing the components of the previously declared variables. If the condition in (3.1) is not satisfied, it can be concluded that two bodies are in contact and normal force can be found as indicated in (3.5).

As mentioned before, the algorithm works with the initial stick assumption by marching tangential relative motion to the next time step while keeping slip motion at the previous step. By defining the displacement vector $\mathbf{\Delta}$ and resultant tension force in the tangential direction P, the following expressions can be obtained.

$$\mathbf{\Delta} = \begin{bmatrix} u_x(\theta_i) - w_x(\theta_{i-1}) \\ u_y(\theta_i) - w_y(\theta_{i-1}) \end{bmatrix}, \tag{3.39}$$

$$P = \sqrt{\mathbf{\Delta}^{\mathrm{T}}.\mathbf{K_t}^{\mathrm{T}}.\mathbf{K_t}.\mathbf{\Delta}} . \tag{3.40}$$

If the following relational operation is satisfied, the stick state is assured.

$$P < \mu n(\theta_i). \tag{3.41}$$

For the stick state, slip motion at θ_i is the same with the slip motion at the previous step, and tangential friction force can be found by the following expression.

$$w_x(\theta_i) = w_x(\theta_{i-1}), \tag{3.42}$$

$$w_y(\theta_i) = w_y(\theta_{i-1}), \tag{3.43}$$

$$\begin{bmatrix} f_{t_x}(\theta_i) \\ f_{t_y}(\theta_i) \end{bmatrix} = \mathbf{K_t}\mathbf{\Delta}. \tag{3.44}$$

In the opposite case of (3.41), slip state occurs. Tangential friction forces and slip motions in both directions can be expressed as follows,

$$\begin{bmatrix} f_{t_x}(\theta_i) \\ f_{t_y}(\theta_i) \end{bmatrix} = \mu n(\theta_i)\frac{\mathbf{K_t}.\mathbf{\Delta}}{|\mathbf{K_t}.\mathbf{\Delta}|}, \tag{3.45}$$

$$\begin{bmatrix} w_x(\theta_i) \\ w_y(\theta_i) \end{bmatrix} = \begin{bmatrix} u_x(\theta_i) \\ u_y(\theta_i) \end{bmatrix} - \mathbf{K_t}^{-1}.\begin{bmatrix} f_{t_x}(\theta_i) \\ f_{t_y}(\theta_i) \end{bmatrix}. \tag{3.46}$$

This algorithm also needs to be repeated until convergence is reached. However, since the convergence which is checked by the relative error on the tangential force highly depends on the threshold value, the threshold error of 10^{-8} may cause hundreds of AFT cycles which increases computational time drastically. Thus, the threshold value should be tuned to comprisable values like 10^{-3} by considering the solution accuracy.

3.1.3.1 Analytical Jacobian for 2D Dry Friction Element with Normal Load Variation

Due to the increased number of DOFs and convergence problems that occurred in the 2D dry friction element with normal load variation, implementing analytical Jacobian formulation becomes a must. The solution needs to be expressed in normal direction as indicated in (3.12), and tangential directions as shown below,

$$u_x(\theta_i) = u_{x0} + \sum_{m=1}^{N_h}\left(u_{x_{s_m}}\sin(m\theta) + u_{x_{c_m}}\cos(m\theta)\right), \tag{3.47}$$

$$u_y(\theta_i) = u_{y0} + \sum_{m=1}^{N_h}\left(u_{y_{s_m}}\sin(m\theta) + u_{y_{c_m}}\cos(m\theta)\right). \tag{3.48}$$

For stick state, (3.44) needs to be changed slightly so that the slip motion term is removed from the equation.

$$f_{t_x}(\theta_i) = \begin{bmatrix} k_{xx} & k_{xy} \end{bmatrix}\begin{bmatrix} u_x(\theta_i) - u_x(\theta_{i-1}) \\ u_y(\theta_i) - u_y(\theta_{i-1}) \end{bmatrix} + f_{t_x}(\theta_{i-1}), \tag{3.49}$$

$$f_{t_y}(\theta_i) = \begin{bmatrix} k_{yx} & k_{yy} \end{bmatrix}\begin{bmatrix} u_x(\theta_i) - u_x(\theta_{i-1}) \\ u_y(\theta_i) - u_y(\theta_{i-1}) \end{bmatrix} + f_{t_y}(\theta_{i-1}). \tag{3.50}$$

From now on, derivation of only $f_{t_x}(\theta_i)$ and $n(\theta_i)$ will be handled with respect to the Fourier coefficients of u_x and v. The reason of omitting y direction is not to make formulation crowded. Formulation with respect to y direction can be deduced from the following equations by changing the corresponding subindexes from x to y.

Derivation of (3.49) with respect to the Fourier coefficients of tangential and normal relative motions,

$$\frac{\partial f_{t_x}(\theta_i)}{\partial u_{x_0}} = \frac{\partial f_{t_x}(\theta_{i-1})}{\partial u_{x_0}}, \tag{3.51}$$

$$\frac{\partial f_{t_x}(\theta_i)}{\partial v_0} = \frac{\partial f_{t_x}(\theta_{i-1})}{\partial v_0}, \tag{3.52}$$

$$\frac{\partial f_{t_x}(\theta_i)}{\partial u_{x_{s_m}}} = k_{xx}\left(\sin(m\theta_i) - \sin(m\theta_{i-1})\right) + \frac{\partial f_{t_x}(\theta_{i-1})}{\partial u_{x_{s_m}}}, \tag{3.53}$$

$$\frac{\partial f_{t_x}(\theta_i)}{\partial v_{s_m}} = \frac{\partial f_{t_x}(\theta_{i-1})}{\partial v_{s_m}}, \tag{3.54}$$

$$\frac{\partial f_{t_x}(\theta_i)}{\partial u_{x_{c_m}}} = k_{xx}\left(\cos(m\theta_i) - \cos(m\theta_{i-1})\right) + \frac{\partial f_{t_x}(\theta_{i-1})}{\partial u_{x_{c_m}}}, \tag{3.55}$$

$$\frac{\partial f_{t_x}(\theta_i)}{\partial v_{c_m}} = \frac{\partial f_{t_x}(\theta_{i-1})}{\partial v_{c_m}}. \tag{3.56}$$

For slip state, (3.45) should be written by separating the force components before derivation.

$$f_{t_x}(\theta_i) = \mu n(\theta_i) \cdot \frac{e_x}{\sqrt{e_x^2 + e_y^2}}, \tag{3.57}$$

$$f_{t_y}(\theta_i) = \mu n(\theta_i) \cdot \frac{e_y}{\sqrt{e_x^2 + e_y^2}}, \tag{3.58}$$

where,

$$e_x = \begin{bmatrix} k_{xx} & k_{xy} \end{bmatrix} \begin{bmatrix} u_x(\theta_i) - u_x(\theta_{i-1}) \\ u_y(\theta_i) - u_y(\theta_{i-1}) \end{bmatrix} + f_{t_x}(\theta_{i-1}), \tag{3.59}$$

$$e_y = \begin{bmatrix} k_{yx} & k_{yy} \end{bmatrix} \begin{bmatrix} u_x(\theta_i) - u_x(\theta_{i-1}) \\ u_y(\theta_i) - u_y(\theta_{i-1}) \end{bmatrix} + f_{t_y}(\theta_{i-1}). \tag{3.60}$$

By using the chain rule, partial derivatives of f_{t_x} can be computed.

$$\frac{\partial f_{t_x}(\theta_i)}{\partial u_{x0}} = \frac{\partial f_{t_x}(\theta_i)}{\partial e_x}\frac{\partial e_x}{\partial u_{x0}} + \frac{\partial f_{t_x}(\theta_i)}{\partial e_y}\frac{\partial e_y}{\partial u_{x0}}$$

$$= \frac{\mu n(\theta_i).e_y}{\sqrt{\left(e_x^2 + e_y^2\right)^3}}\left(e_y\frac{\partial f_{t_x}(\theta_{i-1})}{\partial u_{x0}} - e_x\frac{\partial f_{t_y}(\theta_{i-1})}{\partial u_{x0}}\right), \tag{3.61}$$

$$\frac{\partial f_{t_x}(\theta_i)}{\partial v_0} = \frac{\partial f_{t_x}(\theta_i)}{\partial n(\theta_i)}\frac{\partial n(\theta_i)}{\partial v_0} + \frac{\partial f_{t_x}(\theta_i)}{\partial e_x}\frac{\partial e_x}{\partial v_0} + \frac{\partial f_{t_y}(\theta_i)}{\partial e_y}\frac{\partial e_y}{\partial v_0}$$

$$= \mu k_v\frac{e_x}{\sqrt{e_x^2 + e_y^2}} + \frac{\mu n(\theta_i).e_y}{\sqrt{\left(e_x^2 + e_y^2\right)^3}}\left(e_y\frac{\partial f_{t_x}(\theta_{i-1})}{\partial v_0} - e_x\frac{\partial f_{t_y}(\theta_{i-1})}{\partial v_0}\right), \tag{3.62}$$

$$\frac{\partial f_{t_x}(\theta_i)}{\partial u_{x_{s_m}}} = \frac{\partial f_{t_x}(\theta_i)}{\partial e_x}\frac{\partial e_x}{\partial u_{x_{s_m}}} + \frac{\partial f_{t_x}(\theta_i)}{\partial e_y}\frac{\partial e_y}{\partial u_{x_{s_m}}}$$

$$= \frac{\mu n(\theta_i).e_y}{\sqrt{\left(e_x^2 + e_y^2\right)^3}}\cdot\left[\begin{array}{c}e_y\left(k_{xx}\left(\sin(m\theta_i) - \sin(m\theta_{i-1})\right) + \dfrac{\partial f_{t_x}(\theta_{i-1})}{\partial u_{x_{s_m}}}\right) \\ -e_x\left(k_{yx}\left(\sin(m\theta_i) - \sin(m\theta_{i-1})\right) + \dfrac{\partial f_{t_y}(\theta_{i-1})}{\partial u_{x_{s_m}}}\right)\end{array}\right], \tag{3.63}$$

$$\frac{\partial f_{t_x}(\theta_i)}{\partial v_{s_m}} = \frac{\partial f_{t_x}(\theta_i)}{\partial n(\theta_i)}\frac{\partial n(\theta_i)}{\partial v_{s_m}} + \frac{\partial f_{t_x}(\theta_i)}{\partial e_x}\frac{\partial e_x}{\partial v_{s_m}} + \frac{\partial f_{t_y}(\theta_i)}{\partial e_y}\frac{\partial e_y}{\partial v_{s_m}}$$

$$= \mu k_v\sin(m\theta_i)\frac{e_x}{\sqrt{e_x^2 + e_y^2}} \tag{3.64}$$

$$+ \frac{\mu n(\theta_i).e_y}{\sqrt{\left(e_x^2 + e_y^2\right)^3}}\left(e_y\frac{\partial f_{t_x}(\theta_{i-1})}{\partial v_{s_m}} - e_x\frac{\partial f_{t_y}(\theta_{i-1})}{\partial v_{s_m}}\right),$$

$$\frac{\partial f_{t\,x}(\theta_i)}{\partial u_{x_{c\,m}}} = \frac{\partial f_{t\,x}(\theta_i)}{\partial e_x}\frac{\partial e_x}{\partial u_{x_{c\,m}}} + \frac{\partial f_{t\,x}(\theta_i)}{\partial e_y}\frac{\partial e_y}{\partial u_{x_{c\,m}}}$$

$$= \frac{\mu n(\theta_i).e_y}{\sqrt{\left(e_x^{\,2}+e_y^{\,2}\right)^3}}.\begin{bmatrix} e_y\left(k_{xx}\left(\cos(m\theta_i)-\cos(m\theta_{i-1})\right)+\dfrac{\partial f_{t\,x}(\theta_{i-1})}{\partial u_{x_{c\,m}}}\right) \\ -e_x\left(k_{yx}\left(\cos(m\theta_i)-\cos(m\theta_{i-1})\right)+\dfrac{\partial f_{t\,y}(\theta_{i-1})}{\partial u_{x_{c\,m}}}\right) \end{bmatrix}, \quad (3.65)$$

$$\frac{\partial f_{t\,x}(\theta_i)}{\partial v_{c\,m}} = \frac{\partial f_{t\,x}(\theta_i)}{\partial n(\theta_i)}\frac{\partial n(\theta_i)}{\partial v_{c\,m}} + \frac{\partial f_{t\,x}(\theta_i)}{\partial e_x}\frac{\partial e_x}{\partial v_{c\,m}} + \frac{\partial f_{t\,y}(\theta_i)}{\partial e_y}\frac{\partial e_y}{\partial v_{c\,m}}$$

$$= \mu k_v \cos(m\theta_i)\frac{e_x}{\sqrt{e_x^{\,2}+e_y^{\,2}}} \quad (3.66)$$

$$+ \frac{\mu n(\theta_i).e_y}{\sqrt{\left(e_x^{\,2}+e_y^{\,2}\right)^3}}\left(e_y\frac{\partial f_{t\,x}(\theta_{i-1})}{\partial v_{c\,m}} - e_x\frac{\partial f_{t\,y}(\theta_{i-1})}{\partial v_{c\,m}}\right).$$

For the separation case, since tangential and normal forces are both zero, all partial derivatives of these force components are zero.

$$\frac{\partial f_{t\,x}(\theta_i)}{\partial u_{x_0}} = \frac{\partial f_{t\,x}(\theta_i)}{\partial v_0} = \frac{\partial f_{t\,x}(\theta_i)}{\partial u_{x_{s\,m}}} = \frac{\partial f_{t\,x}(\theta_i)}{\partial v_{s\,m}} = \frac{\partial f_{t\,x}(\theta_i)}{\partial u_{x_{c\,m}}} = \frac{\partial f_{t\,x}(\theta_i)}{\partial v_{c\,m}} = 0, \quad (3.67)$$

$$\frac{\partial n(\theta_i)}{\partial u_{x_0}} = \frac{\partial n(\theta_i)}{\partial v_0} = \frac{\partial n(\theta_i)}{\partial u_{x_{s\,m}}} = \frac{\partial n(\theta_i)}{\partial v_{s\,m}} = \frac{\partial n(\theta_i)}{\partial u_{x_{c\,m}}} = \frac{\partial n(\theta_i)}{\partial v_{c\,m}} = 0. \quad (3.68)$$

Up to now in this part, partial derivatives of the tangential friction force are formulated for slip and stick states. For both states, the normal force can be calculated as (3.10). Partial derivation of (3.10) with respect to v_0, $v_{s\,m}$ and $v_{c\,m}$ yields the same expressions as (3.26) to (3.28). Similarly, derivations with respect to u_0, $u_{x_{s\,m}}$ and $u_{x_{c\,m}}$ are zero as in 1D case which can be seen from (3.29) because normal forcing doesn't include these Fourier coefficients related with tangential motion.

After calculating partial derivation of each force component with respect to all Fourier coefficients corresponding to the nonlinear DOFs in the displacement vector in the time domain, these derivations should be transformed to the frequency domain as indicated in (3.30) to (3.33).

3.2 Fretting Wear Modelling

3.2.1 Archard's Model

Archard's model is one of the earliest approach used in the literature. According to the model, wear occurs during the fracture of asperities formed between contacting surfaces.

$$Q = k.A_R \, , \tag{3.69}$$

where Q is the wear rate, A_R is the contact area which is defined as $A_R = \dfrac{N_0}{H}$. Physically $\dfrac{N_0}{H}$ term represents the real contact area for fully plastic asperities according to Tabor's definition of hardness. It should be kept in mind that the above formulation can be applied to both Archard's adhesive model and Rabinowicz's abrasive model.

$$\frac{V}{s} = k \frac{N_0}{H} , \tag{3.70}$$

where k is the dimensionless wear coefficient, N_0 is the normal force, H is the hardness of the material, s is the sliding distance, and V is the volume of the wear particles. Note that the wear coefficient is determined experimentally. Local wear depth can also be found from the following formula,

$$dh(x,t) = \frac{k}{H} p(x,t).ds(x,t), \tag{3.71}$$

where p is the contact pressure, ds is the slip increment, and dh is the local wear depth.

In the original Archard model flow pressure term is used instead of the hardness term. However, by the work of Kassman et al. [36], the Archard model is modified such that the pressure term is replaced by the hardness term.

It is important to note that the wear coefficient and the friction coefficient are strongly dependent on displacement amplitude, contact force, and wear mode which results in different Archard's wear coefficients for each experiment conducted. Also, various studies have shown that the wear coefficient increases when the elastic shakedown boundary is crossed, and the coefficient of friction should be integrated for the alternating sliding distance problems. However, Archard's formulation doesn't include the coefficient of friction which is the deficiency of the model.

3.2.2   Wear-Energy Approach

Studies by Fouvry et al. [24]–[26] demonstrated that there is a linear relationship between material removal and the dissipated friction energy. Note that this model is analogous to Theodor Reye's model which is one of the first wear models that considers wear from the energy standpoint. It is known that the area inside the hysteresis loop corresponds to the energy dissipation per cycle and total energy dissipation is the sum of energy dissipation of each cycle. The advantage of the wear-energy approach over Archard's model is that change in the coefficient of friction is also included to the model indirectly since energy dissipation is directly calculated from the measured area inside the hysteresis loop which can be seen from the dashed area below.
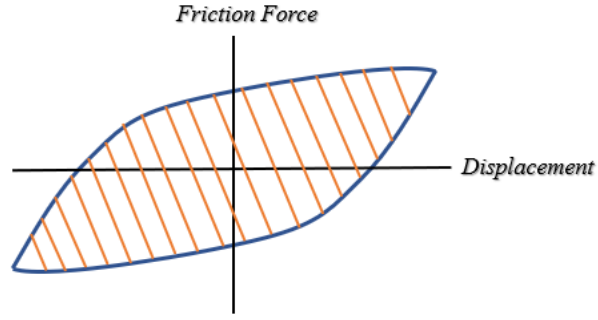
Figure 3.4 Typical Hysteresis Loop

Let the orange dashed area in Figure 3.4 be E_n which is the fretting energy dissipated over one cycle. Then, wear depth can be calculated as follows,

$$V = \alpha \sum_{n=1}^{N_c} E_n,$$
(3.72)

where α is the wear coefficient, N_c is the number of friction cycles, and V is the wear volume. Careful investigation will reveal that during the gross slip regime, Archard and energy-wear coefficients are the same, i.e. $\alpha/\mu = k/H$. However, during the partial slip where friction force is smaller than the limiting value (μn), the two approaches are not the same unless k/H is modified.

3.2.3   Atomic Scale Approach

In recent years atomic scale approaches are also used instead of macro-scale classical approaches. The wear coefficient k is a function of the scaling of the model. Bassani et al. [27] worked on adhesive contact condition in atomic scale model where dragging of atoms are assumed to be the reason for wear.

$$k = \frac{\omega_t . V_{at}}{A_{R/n} . V_s},$$
(3.73)

where, ω_t is the transition rate found by Arrhenius law, V_{at} is the atomic debris volume, $A_{R/n}$ is the specific area per contact atom, and V_s is the scanning speed of the asperity. By combining (3.73) with (3.69), the wear rate Q can be expressed in atomic scale form as,

$$Q = \frac{\omega_t . V_{at} . A_R}{A_{R/n} . V_s} .$$
(3.74)

However, all these constants need experiments and specialized models which are still scarce and difficult to apply to a real engineering problem.

CHAPTER 4

ALGORITHM FOR FRETTING WEAR CALCULATION COUPLED WITH FRICTION CONTACT MODEL

In this chapter, 1D dry friction element with normal load variation induced by normal motion and wear-energy approach which are discussed in the previous section are coupled to analyze the effect of fretting wear on the wear estimation at the contact surface and dynamic response of the system. The methodology is discussed from two perspectives based on a multiscale approach.

4.1   Algorithm Based on Wear Depth

In the wear-energy approach, wear volume for one friction cycle can be calculated by the multiplication of the energy dissipated by the friction contact in a single cycle and a wear coefficient which is determined experimentally. Since fretting wear models discussed in the previous sections are defined as microscale phenomena, energy should be calculated by integrating the multiplication of shear and velocity distribution over the contact surface. By this way, wear is calculated on the distributed surface. However, in the macroslip friction models which are discussed in the 3.1 and used in this thesis work, energy is calculated at each contact node respectively, and consequently, wear depth at each node is obtained individually. Thus, energy dissipation, shear stress, and wear depth are assumed to be constant in a small square area which is determined by the edge length of the element used in the FEM. Denoting this square area as A_p and rewriting (3.72) to find the wear depth at the contact node region, the following equation can be obtained.

$$\delta = \frac{\alpha}{A_p} \sum_{n=1}^{N_c} E_n.$$

(4.1)

E_n should be obtained from the input displacement and the resulting tangential friction force. For single harmonic motion, displacement and the tangential friction force can be written by the reference of (3.11) as follows,

$$u = u_0 + u_s \sin(\omega t) + u_c \cos(\omega t), \tag{4.2}$$

$$f_n = f_{n_0} + f_{n_s} \sin(\omega t) + f_{n_c} \cos(\omega t), \tag{4.3}$$

By omitting bias term which has no effect on the dissipated energy, (4.2) and (4.3) can be written alternatively as follows,

$$u = Y \sin(\psi) = Y \sin(\omega t - \phi), \tag{4.4}$$

$$f_n = f_{n_s}^* \sin(\psi) + f_{n_c}^* \cos(\psi), \tag{4.5}$$

where, Y is the amplitude and ϕ is the initial phase angle for sinusoidal motion.

$$Y = \sqrt{u_s^2 + u_c^2}, \tag{4.6}$$

$$\phi = -atan2\left(\frac{u_c}{u_s}\right), \tag{4.7}$$

$$f_{n_s}^* = f_{n_s} \cos(\phi) - f_{n_c} \sin(\phi), \tag{4.8}$$

$$f_{n_c}^* = f_{n_s} \sin(\phi) + f_{n_c} \cos(\phi). \tag{4.9}$$

While the sine term of the forcing $\left(f_{n_s}^*\right)$ behaves like an elastic spring for the stick status of the interface, the cosine term of the forcing $\left(f_{n_c}^*\right)$ adds additional damping to the system during the slip state of the interface. Obviously, the separation state bypasses both stiffening and damping effects by zeroing force term. Thus, instead of the sine term of the forcing which has a restoring force, the cosine term of the forcing should be considered for the evaluation of the energy dissipation due to friction

damping. Dissipated energy can be calculated with the integral of the power which is force times velocity over one cycle.

$$\dot{u} = Y\cos(\psi), \tag{4.10}$$

$$E_n = \frac{1}{\omega} \int_0^{2\pi} f_{n_c}^* \cos(\psi)\dot{u}\, d\theta = \pi Y f_{n_c}^*. \tag{4.11}$$

Since wear is assumed to be a slow-scale phenomenon compared to the dynamic characteristics and dimensions of the system, nonlinear forced response analysis must be conducted only after a certain amount of wear accumulation is obtained. To determine the number of wear cycles (N_c) before recalculating the dynamic response analysis, a permissible wear depth, (δ_u) which is the update rate of the analysis for single wear iteration, needs to be defined. The number of wear cycles is defined as follows,

$$N_c = \frac{\delta_u}{\max(\boldsymbol{\delta})}, \tag{4.12}$$

where $\boldsymbol{\delta}$ is the nodal wear depth vector for the corresponding wear iteration that includes the nodal wear depth of all the contact points. After finding the number of wear cycles (N_c), the wear depth for each node can be calculated by the multiplication of the wear cycle and the determined nodal wear depth as,

$$\boldsymbol{\delta_{tot}} = \boldsymbol{\delta_{tot}} + N_c\boldsymbol{\delta}, \tag{4.13}$$

where $\boldsymbol{\delta_{tot}}$ represents the cumulative wear depth vector for all contact points. Another important input parameter for wear analysis is the maximum total nodal wear depth (δ_{all}). It's a limiting parameter to stop the whole analysis until the allowable wear depth is reached at any of the contact nodes.

Three main assumptions are done in the wear algorithm:

- The equation of motion (2.1) of the system does not change with the wear occurrence at the contact interface, since the worn volume is very small compared to the total dimensions of the model.
- Energy dissipation due to friction in one cycle, which can be calculated from the area inside the hysteresis loop, is assumed to be constant during a wear iteration, and wear accumulated proportionally.
- System runs at a specific operating frequency which is mostly the resonant frequency where the energy dissipation is the highest.

At this point, how the worn profile is fed back to the nonlinear equation of motion which represents the dynamics of the system should be discussed. Problems with dry friction nonlinearity, mostly friction dampers, are solved by preliminary static analysis to find the normal load distribution along the contact surface. This force field is the input for the Coulomb friction element as a static preload. This uncoupled approach decreases the number of unknowns to be solved in the nonlinear solver. However, there is another method which is called as coupled approach. Here, the static term is also added to the displacement vector so that preliminary static analysis is not needed anymore. Moreover, due to the initial preload/gap term used in the friction model, the built-up gap due to wear modifies normal force through this term and behaves like a negative preload such that the dynamic response is updated after each wear iteration. As discussed before, static term is used in this study and coupled approach is utilized. Inserting the accumulated nodal wear depth $\left(\boldsymbol{\delta}_{\mathbf{tot}}\right)$ to the (3.5), normal force for the reanalysis of the nonlinear system can be updated in the AFT algorithm as follows,

$$n(\theta) = n_0 + k_v \left(v(\theta) - \delta_{tot}\right). \tag{4.14}$$

Figure 4.1 gives good summarization of the flowchart of the algorithm. As seen, the number of wear cycles is indirectly calculated from the update rate input which is why this approach is called as wear depth perspective. This algorithm is introduced

to give an idea about how the presumed wear depth value changes the dynamic response of the system.
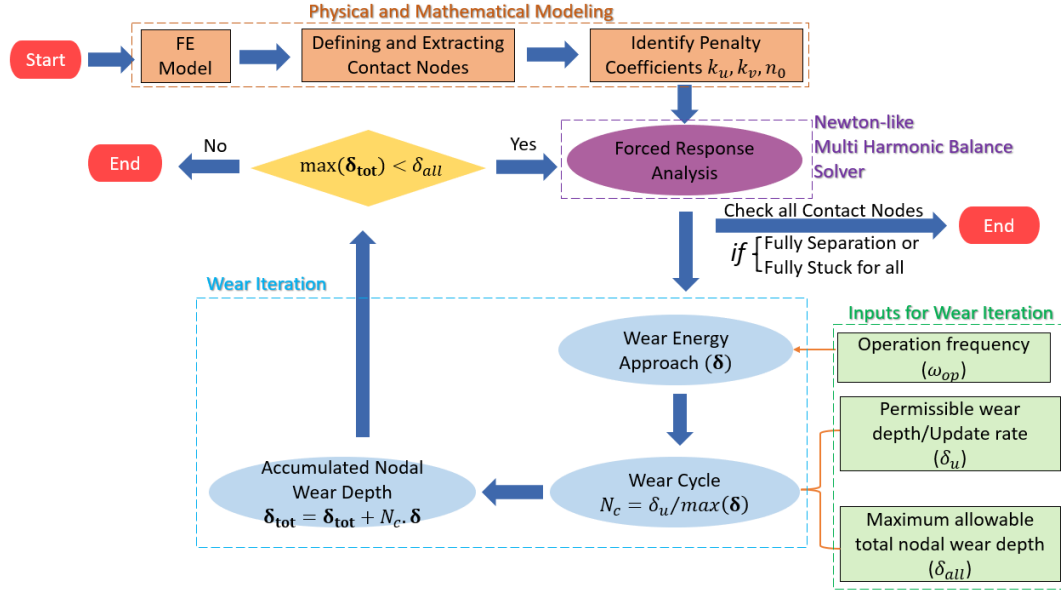

Figure 4.1 Flowchart of the Dynamic Response Analysis Coupled with Fretting Wear from the Wear Depth Perspective

4.2 Algorithm Based on Wear Cycle

Most of the time, the main reason for investigating fretting wear and its effect on the dynamic response of the overall system is to foresee the maintenance intervals of the working components. By this way, good insight can be achieved about the lifetime and maintenance period prediction so that design parameters like material and dimensions of the structure might be tuned accordingly which is mostly the real engineering standpoint. Hence, the previous algorithm is slightly changed by omitting (4.12) just after the calculation of wear depth at each node ($\boldsymbol{\delta}$) since wear cycle (N_c) is an input parameter for wear iteration. By this way, accumulated nodal wear depth $\left(\boldsymbol{\delta_{tot}}\right)$ can be calculated by the input wear cycle parameter in (4.13).

As the flowchart is schematically illustrated in Figure 4.2, the limiting parameter to terminate the algorithm is denoted with $N_{c_{all}}$. If the parameter i_w is denoted to count

the number of wear iterations, the last forced response analysis before terminating

the algorithm would occur when $i_w = \dfrac{N_{c_{all}}}{N_c}$. It is also worth mentioning the

correlation between the operation time with $N_{c_{all}}$ in cycles and ω_{op} in rad/s.

$$t_h = \frac{N_{c_{all}}}{3600.\omega_{op}} \tag{4.15}$$
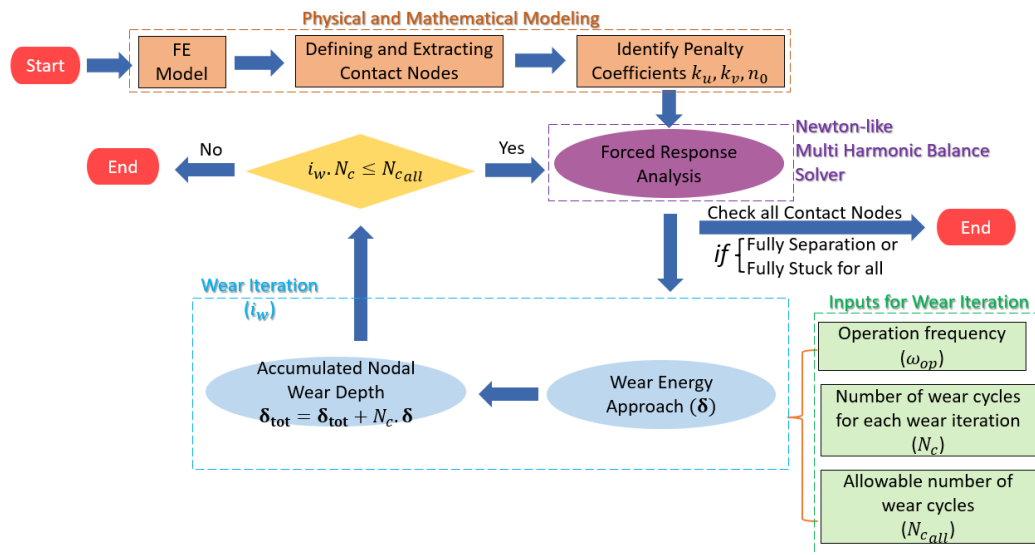
where t_h is the operation time in hours.

Figure 4.2 Flowchart of the Dynamic Response Analysis Coupled with Fretting
Wear from the Wear Cycle Perspective

CHAPTER 5

NUMERICAL CASE STUDIES

5.1 Shrouded Blade

The Computer-Aided Drawing (CAD) model of the shrouded blade case study is shown in Figure 5.1. Points A, B, and C represent the preload force node, excitation node, and contact nodes respectively. The surface denoted with D represents the fixed support of the structure. Note that, response is the average of all contact nodes at the contact interface.
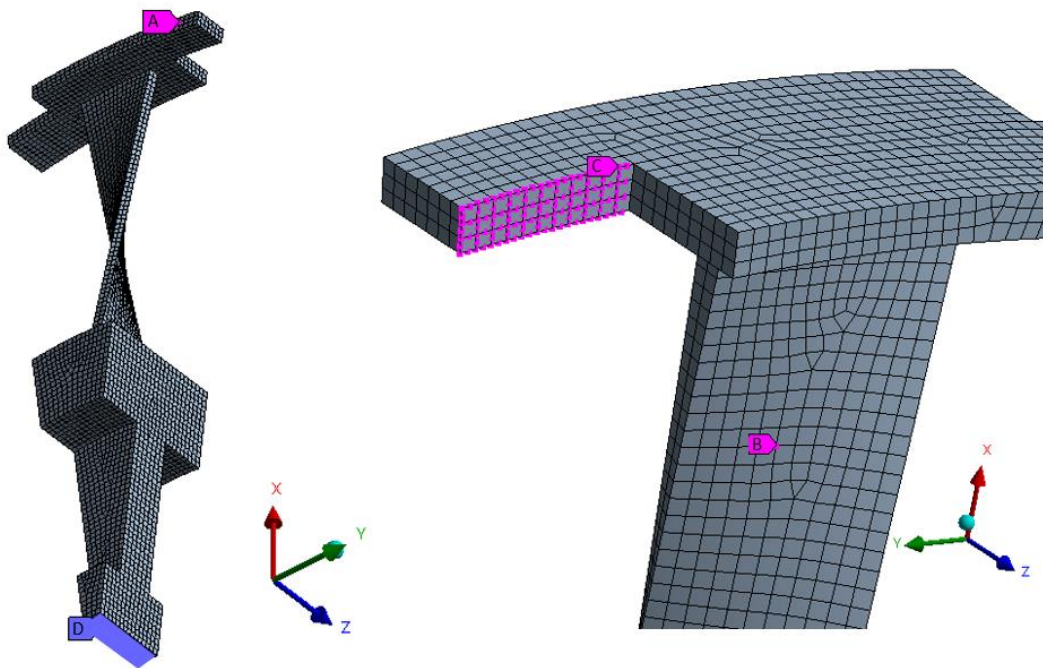
Figure 5.1 CAD Model of the Shrouded Blade

Table 5.1 Parameters of the Shrouded Blade Model

Material	Steel
Elastic Modulus	$200\ GPa$
Density	$7.85 \times 10^{-6}\ kg/mm^3$
Excitation Force Amplitude	$1\ N$ in -*y* direction
Preload Force	To be determined
Structural Damping	0.01
Contact Surface Dimensions	$5 \times 21\ mm$
Number of Contact Nodes	121
Tangential Contact Stiffness	$\begin{bmatrix} 100 & 25 \\ 25 & 100 \end{bmatrix} N/m$
Normal Contact Stiffness	$100\ N/m$
Coefficient of Friction	0.5
Wear-Energy Coefficient	$2 \times 10^3\ \mu m^3/J$

In Table 5.1, input analysis parameters are shown. As seen from the table, the normal force is left to be decided after preliminary nonlinear forced response analysis. This parameter should be chosen in such a way that, while response at the damped natural frequency is kept at relatively low levels, the damped natural frequency shifting characteristic during the wear process that decreases the normal load distribution over the contact surface should be taken into account.

To determine the proper normal load value, dynamic responses for various excitation over normal force is analyzed and plotted in Figure 5.2. As seen from the figure, the damped response abruptly increases for the cases above $\frac{1}{10}$ and $\frac{1}{15}$. Thus, after a visual inspection, preload value can be chosen as $20\,N$, since while the damped response is relatively at low amplitudes, the effect of leftward damped frequency shifting due to negative preload is designed not to affect the damping performance of the damper drastically.
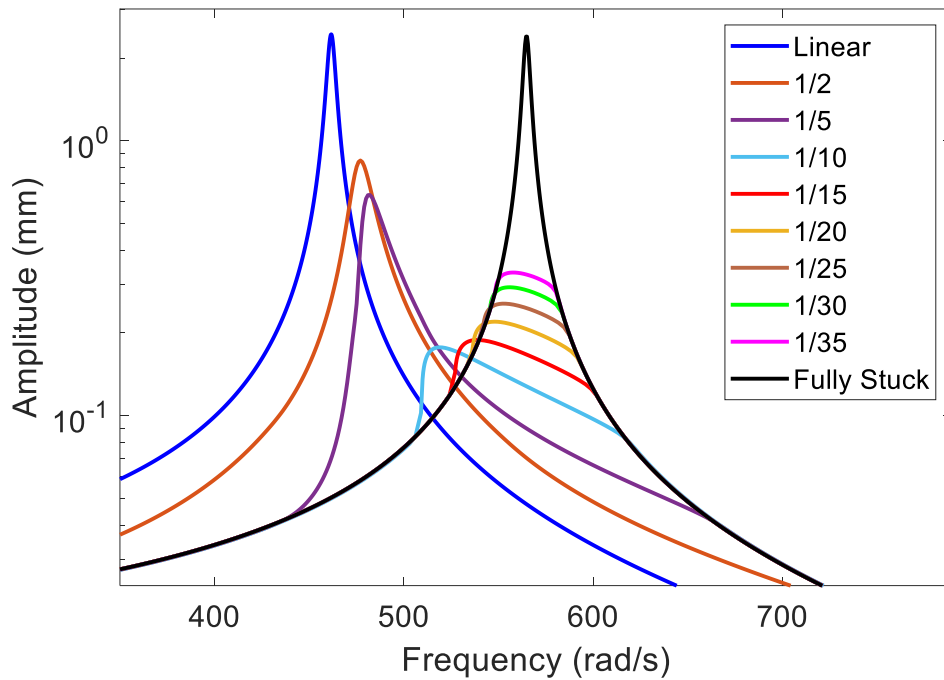
Figure 5.2 Frequency Response for Various Excitation over Preload Values

The operating frequency of the damper can be similarly chosen from Figure 5.2. To speed up and see the effect of wear, the frequency value of $560\,rad/s$ which corresponds to the approximately maximum amplitude can be chosen.

When the dimensions of the contact patch are considered, the permissible wear depth for each wear iteration $\left(\delta_u\right)$ is decided to be $0.002\,mm$. On the other side, the maximum allowable total nodal wear depth $\left(\delta_{all}\right)$ which is the breaking condition for the whole wear analysis is chosen to be $0.1\,mm$, $0.2\,mm$ and $0.3\,mm$ to compare the change in the nonlinear dynamic response for different δ_{all} values and plotted in Figure 5.3. The operation time and wear iterations corresponding to different δ_{all} values are also tabulated in Table 5.2.
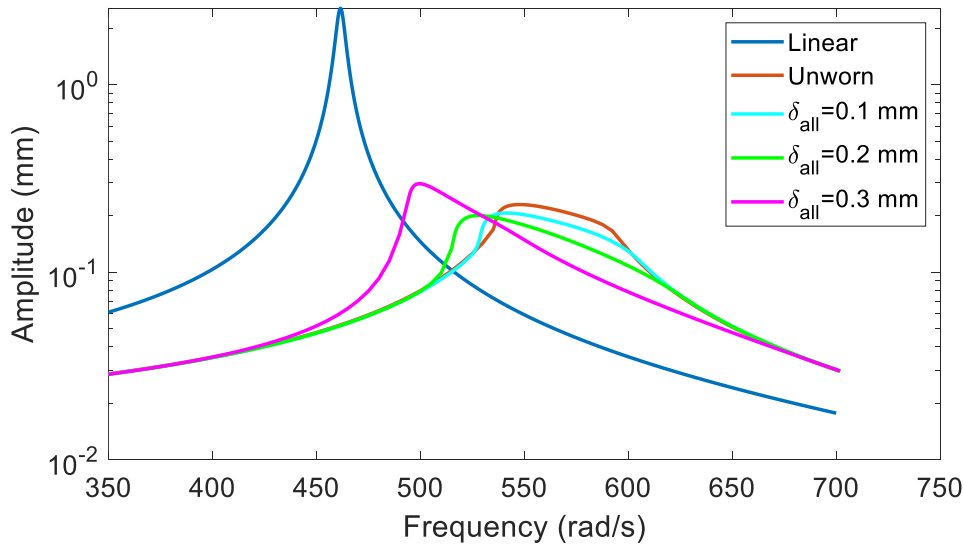
Figure 5.3 Frequency Response of the Worn Profile for Different δ_{all} Values

Table 5.2 Wear Analysis Results

δ_{all}	Total Wear Iterations	Total Number of Cycles	Operation hours
0.1 mm	50	3.7×10^{10}	1.8×10^4
0.2 mm	100	8.4×10^{10}	4.2×10^4
0.3 mm	161	1.7×10^{11}	8.4×10^4

Further, the similarity between Figure 5.2 and Figure 5.3 draws attention. As explained earlier, shifting to the left due to the gap at the worn-out profile (i.e., negative preload) brings softening effect to the system and shifts the nonlinear forced response to the left. In other words, wearing behaves like decreasing the normal force component as the time progressed. Hence, the designer should consider the progressive wear on the dynamic response of the system. Here, choosing normal preload value as $20N$ instead of $10N$ is a more foresightful choice from the engineering perspective although damper performance for $10N$ preload is higher for unworn structure.

Contact status of the interface is an important monitoring tool to have insight about the response of the system before and after the wear process. Figure 5.4 shows the contact status evolution at the interface for $\delta_{all} = 0.2\,mm$, before and after the wearing process. As seen from the figure, the leftmost part of the interface turns into a fully stuck state and the energy dissipation feature is lost at these points. On the other side, stick/slip status is maintained as it's moved towards the right.
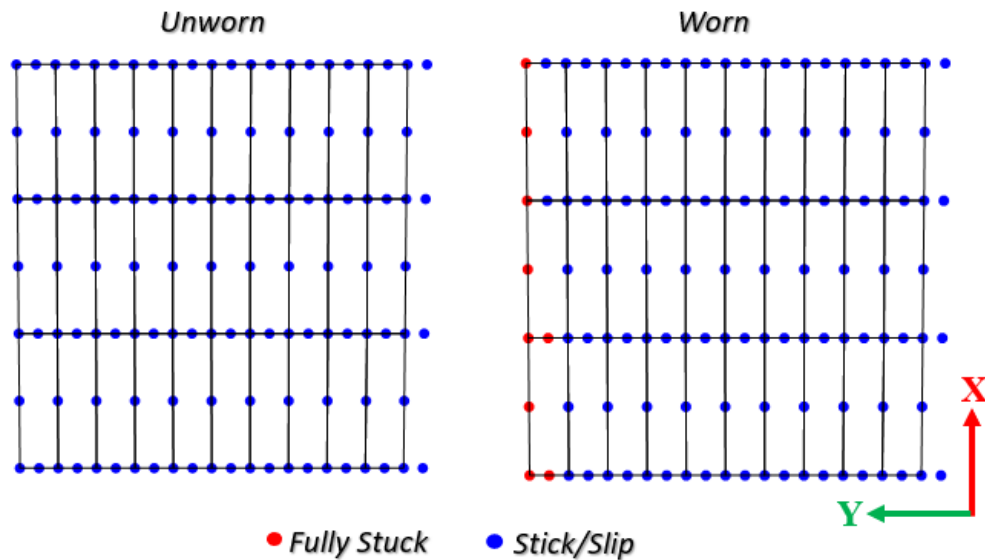
Figure 5.4 Unworn Contact Status and Worn Contact Status for $\delta_{all} = 0.2\,mm$

Although it cannot be monitored in Figure 5.4, it can be deduced that the stick state over one period increases from right to left and this will create a wear pattern. Thereby, it's also beneficial to see the interpolated wear depth over the contact surface by a contour plot, in Figure 5.5. Note that in order to obtain a smooth surface, wear depts obtained are interpolated by the "*griddata*" function of MATLAB. Wear map shows that the leftmost part of the contact surface is less worn, and the wear depth is increased towards the right. The difference between most and least depth corresponds to the $0.14\,mm$. What can be deduced from this result is that for the leftmost points, stick regime dominates over one period when compared with the rightmost regions. As a consequence of a less slip regime, the leftmost region has less energy dissipation and less wear depth.
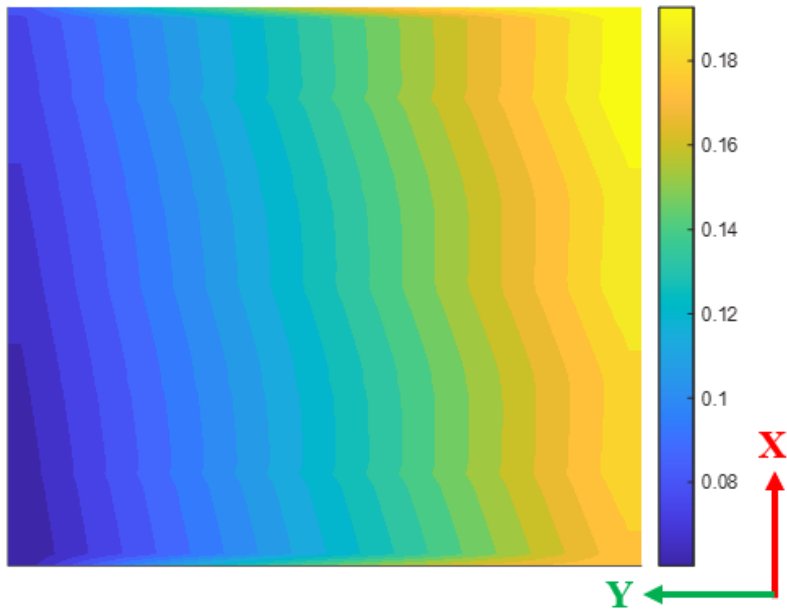
Figure 5.5 2D Wear Map in (mm) for $\delta_{all} = 0.2\ mm$
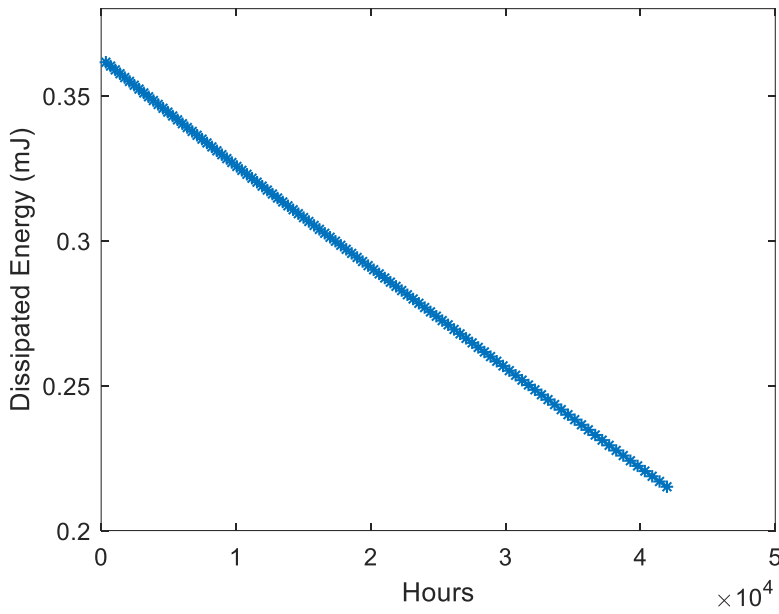

Figure 5.6 Total Dissipated Energy for $\delta_{all} = 0.2\ mm$

Additionally, Figure 5.6 shows expected decrease in total energy dissipation over the operation hours. The graph shows a remarkable decrease of 40 percent less dissipated energy at the operation frequency.

Similarly, Figure 5.7 illustrates the wear process at which δ_{all} reaches to $0.3\ mm$ wear depth. Besides the stick/slip and fully stuck statuses, stick/slip/separation is also observed at the rightmost section of the contact interface. Additionally, the number of contact elements that experience the fully stuck state is increased with increasing operation time.
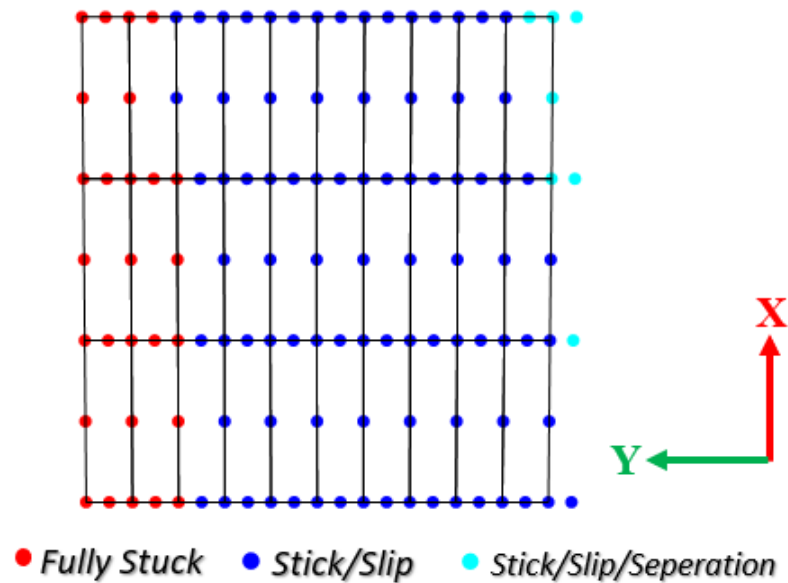
Figure 5.7 Worn Contact Status for $\delta_{all} = 0.3\ mm$

Up to now, how the design region of the damper is disturbed over the time is observed. However, from an academic perspective, running the wear algorithm to the excessive wear depths which is far beyond the sensible levels arouses curiosity. As explained in Figure 4.1, one of the conditions for terminating the algorithm is that all the contact nodes experience separation status. Hence, when the algorithm is run till this condition occurs, it's observed that $\max(\delta)$ reaches the value of $0.45\ mm$ and frequency response at the corresponding wear depth gets closer to the free state response of the structure as shown in Figure 5.8.
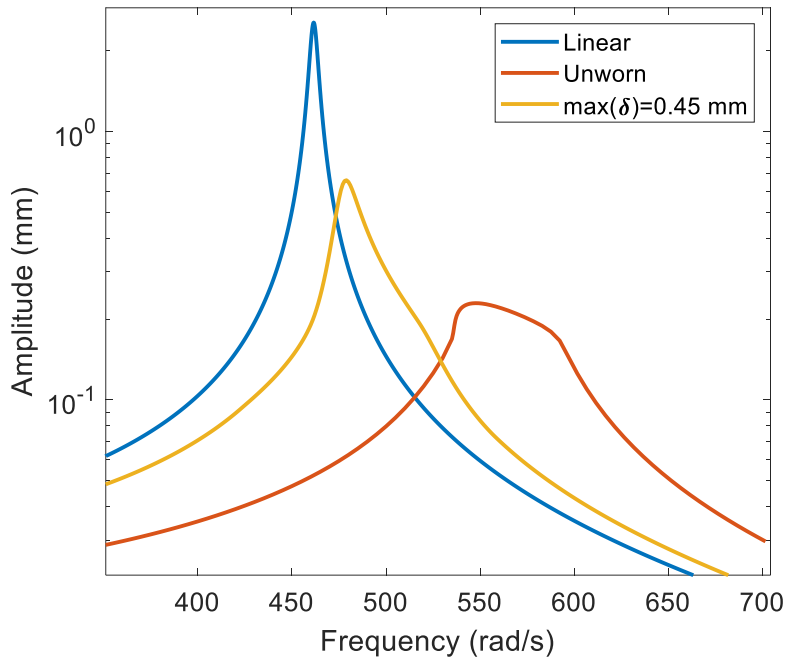
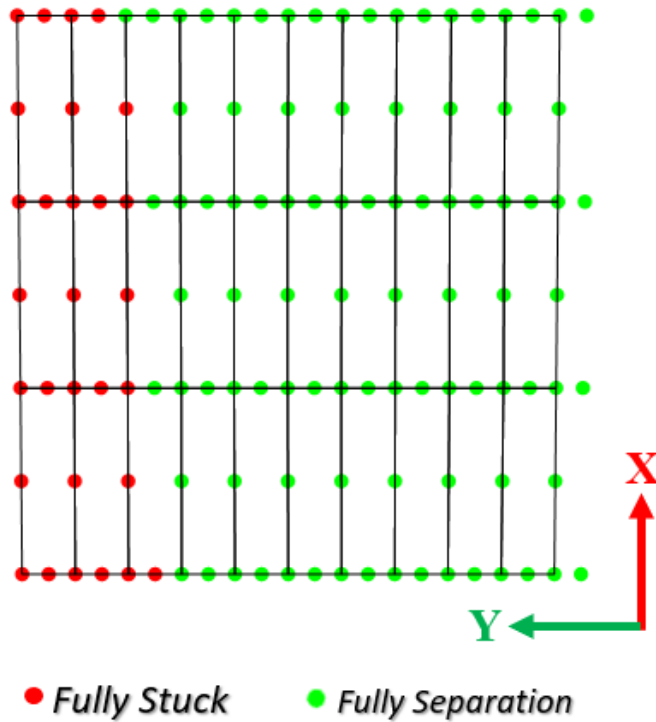Figure 5.8 Frequency Response for $\max(\boldsymbol{\delta}) = 0.45 \, mm$

Figure 5.9 Worn Contact Status for $\max(\boldsymbol{\delta}) = 0.45 \, mm$

As seen in Figure 5.9, contact status for $\max(\boldsymbol{\delta}) = 0.45 \, mm$ is consistent with the previously shown contact status results at the intermediate phases. The contact interface is evolved to a nonfunctional condition since all nodes experiences either fully stuck or fully separation state. As explained earlier, slipping is the only energy dissipation mechanism in the system. However, the worn structure only behaves like an additional spring due to the fully stuck nodes which shift the linear response to the right. The reason for such worn status map is that the rightmost section of the interface is stiffer when compared with the left side, as a result of which the leftmost section ends up with a fully stuck state while the rightmost section fully separates at the operation frequency. Further, these interpretations are verified by the Figure 5.10 which shows the dissipated energy over the years. After $3.5 \times 10^5 \, hours \cong 40 \, years$ of operation, the performance of the damper drops more than 99 percent although that many years of operation without maintenance is not feasible.
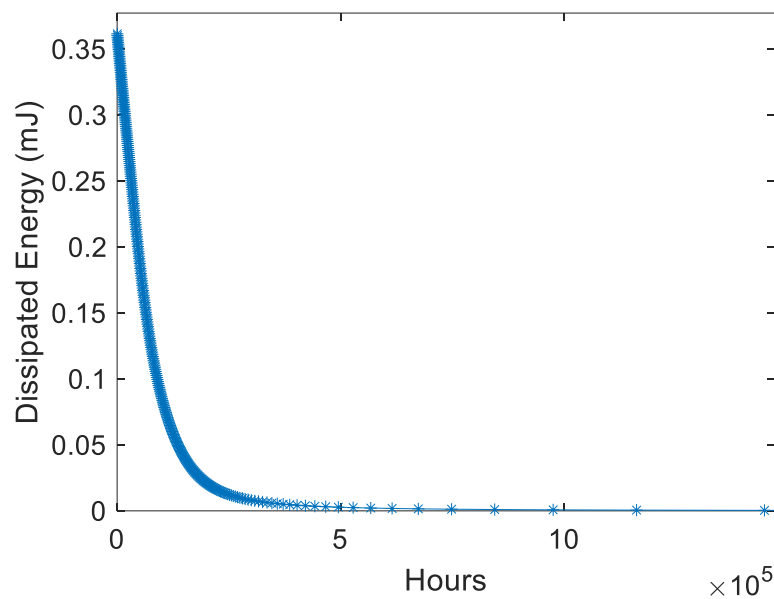

Figure 5.10 Total Dissipated Energy for $\max(\boldsymbol{\delta}) = 0.45 \, mm$

It is also worth mentioning that, as discussed earlier, the accelerated friction cycle (N_c) directly depends on permissible wear depth (δ_u). On the other side, wear iteration is the variable that is counted after each update of the dynamic response

(displacement vector) of the contact nodes. The relationship between these two parameters is plotted in Figure 5.11. Expectedly, the friction cycle to reach permissible wear depth for each iteration increasingly grows with respect to wear iteration. Again, this result verifies that less wear occurs for a single friction cycle as a consequence of less energy dissipation due to dominating sticking and separation regime over slip regime.
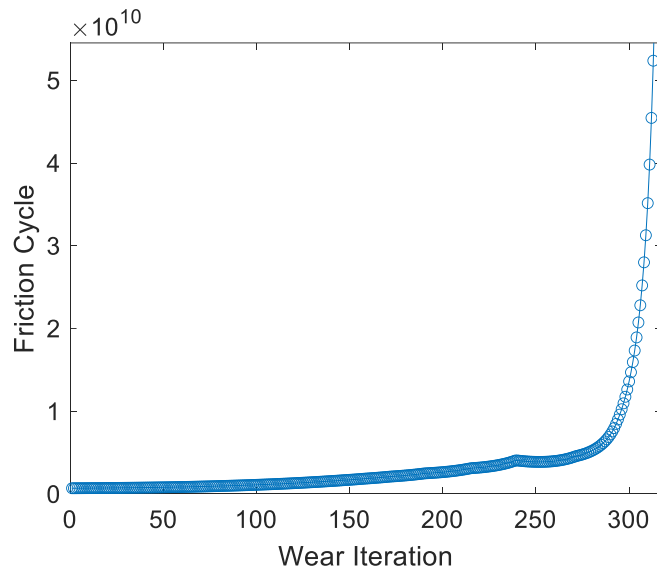

Figure 5.11 Friction Cycles vs. Wear Iteration

Although δ_u is decided to be $0.002\,mm$ for this analysis, the effect of coarse and fine values of δ_u should also be discussed. To analyze this effect, the maximum allowable total nodal wear depth δ_{all} of $0.3\,mm$ is approached with different values of permissible wear depths (δ_u) as summarized in Table 5.3. If $\delta_u = \delta_{all}$, the analysis stops after a single wear iteration which is the coarsest possible choice. While δ_u is getting smaller, accuracy and solution time increases.

Table 5.3 Input Wear Depth Parameters

$\delta_{all}\,(mm)$	0.3					
$\delta_u\,(mm)$	0.3	0.05	0.01	0.005	0.0005	0.0001
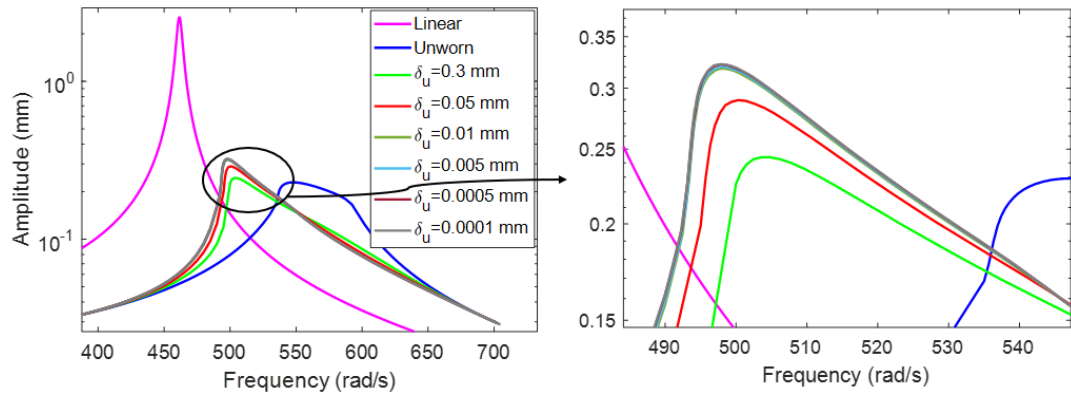
Figure 5.12 Frequency Response for Different δ_u Values

Table 5.4 Results of the Analysis for Different δ_u Values

$\delta_{all}\ (mm)$	0.3					
$\delta_u\ (mm)$	0.3	0.05	0.01	0.005	0.0005	0.0001
Number of Wear Iterations	1	7	33	65	643	3215
Solution Time (sec)	23.22	26.66	38.04	45.20	99.26	404.92

Figure 5.12 shows the nonlinear forced response for different values of permissible wear depth (δ_u). After $\delta_u \leq 0.01\ mm$, frequency response lines almost overlap with each other.

Outputs of Table 5.3 is presented in Table 5.4. While the third row represents the number of wear iterations for each permissible wear depth choice, the fourth row shows the corresponding solution time. Note that, besides the wear loop, solution time also includes the nonlinear forced response analysis just after the wear iteration. In other words, individual wear analysis time for each analysis would be lower than these values.

51

Figure 5.13 is another useful plot to understand the nature of the problem. In the figure, each successive marker corresponds to the relative difference between the summation of the maximum response of each node at the operation frequency. The error tends to decrease as the δ_u getting finer and eventually, it's expected to be zero while δ_u goes to zero.
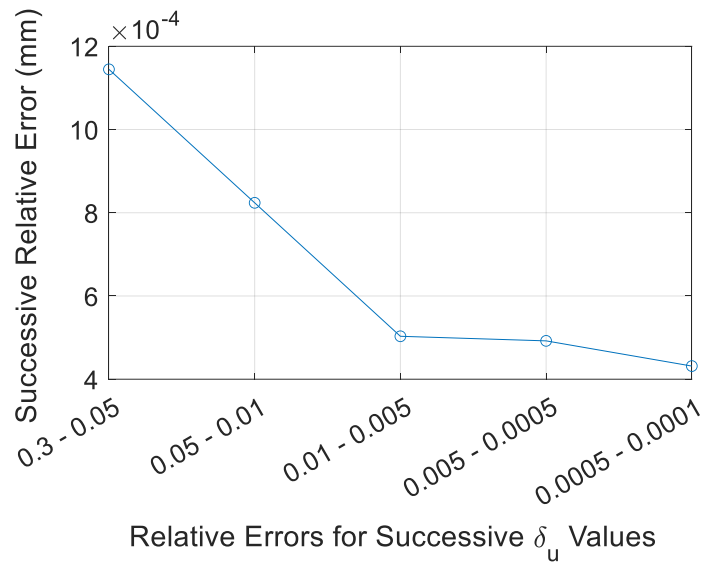

Figure 5.13 Relative Errors for Successive δ_u Values

Thanks to the proposed wear algorithm, acceptable level of solution time and the relatively low successive error between different values of δ_u enables user to choose the optimized δ_u manually and efficiently. Thus, for this case study, $\delta_u = 0.002\ mm$ was a safe side choice throughout the analysis.

5.2 Grounded Blade Platform

In this case study, the effect of the number of macroslip friction elements on the dynamic characteristic and wear pattern of the frictionally damped blade platform is analyzed. The analysis is conducted from two perspectives that are described in

Chapter 4. 1D dry friction element with normal load variation is used to model the contact interface.

The finite element model of the blade platform connected to the ground is given in Figure 5.14 which is a simplified model of a blade with an underplatform damper. Points A, B, C, and D represent the response node, excitation force node, preload nodes, and the contact nodes, respectively. The surface denoted with E shows the area where all DOFs are fixed. Input parameters for the case study are given in Table 5.5.
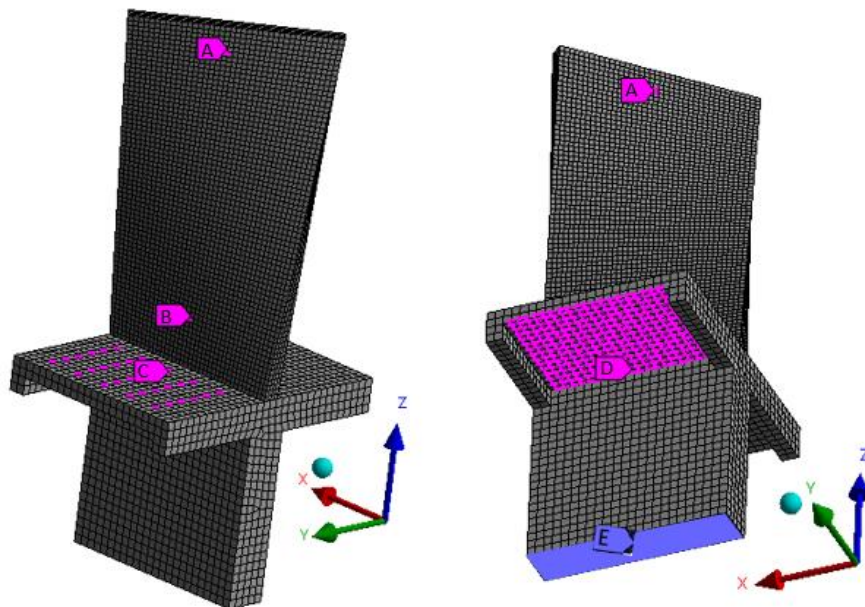

Figure 5.14 CAD Model of the Grounded Blade Platform

Table 5.5 Parameters of the Grounded Blade Platform

Material	Steel
Elastic Modulus	$200\ GPa$
Density	$7.85 \times 10^{-6}\ kg/mm^3$
Excitation Force Amplitude	$500\ N$ in y direction
Preload Force	$1000\ N$ for each node in -z direction (Equally Spaced 30 Nodes)
Structural Damping	0.01
Contact Surface Dimensions	$100 \times 67.5\ mm$
Tangential Contact Stiffness (for 20 Friction Elements)	$1.25 \times 10^6\ N/m$
Normal Contact Stiffness (for 20 Friction Elements)	$1.25 \times 10^6\ N/m$
Coefficient of Friction	0.5
Wear-Energy Coefficient	$2 \times 10^3\ \mu m^3/J$

Distribution of the contact elements on the contact interface is shown in Figure 5.15 for the cases with minimum and maximum number of friction elements. To understand the nature of the problem and choose an operation frequency for the wear analysis, the nonlinear response of the blade tip at Point A, which is defined as a response node, for different preload values is given in Figure 5.16. Note that, no difference is observed between the nonlinear responses of the unworn structure for 20 and 266 friction elements which is the reason why Figure 5.16 is plotted for 20 friction elements.
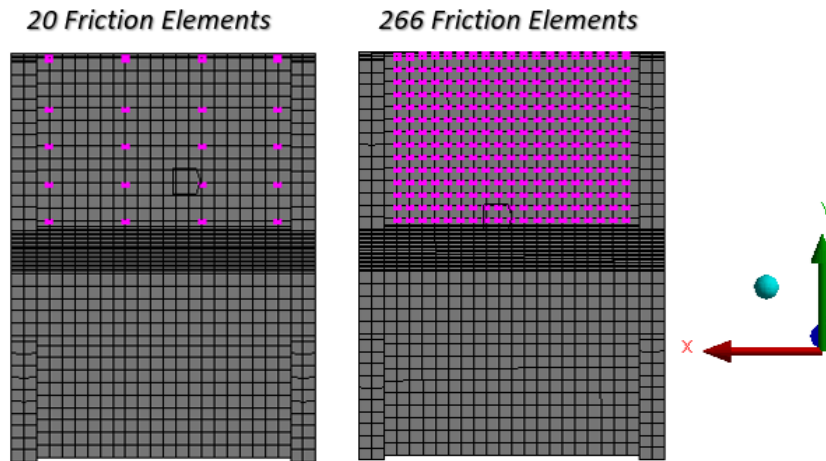
Figure 5.15 Distribution of Friction Elements on the Contact Patch

As seen from the green line in Figure 5.16, $1000\,N$ in -z can be chosen as an optimum value for the preload to use in the case studies. Moreover, the operation frequency of $1115\,rad/s$ is the most critical point for this case corresponding to the maximum amplitude.
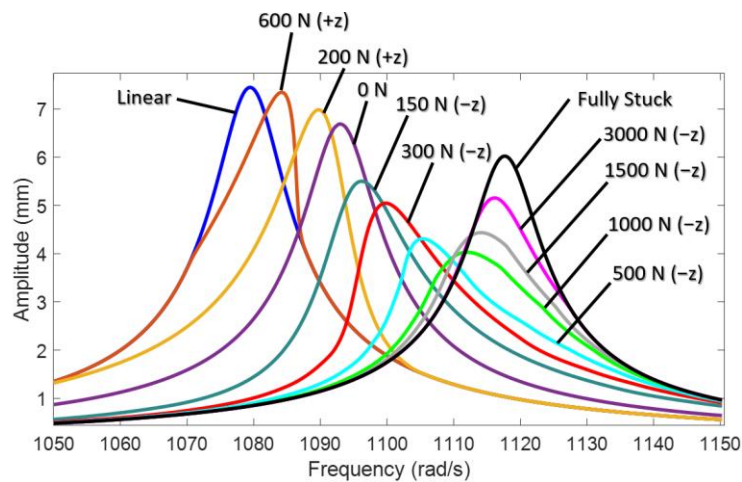

Figure 5.16 Frequency Response for Different Preload Values

At this point, inevitable usage of analytical Jacobian which is introduced in Section 3.1.2.1 needs to be discussed. Although implementing numerical Jacobian to the solver extremely simplifies the formulation, it causes drastic increase in solution time especially when the number of contact elements is high. Hence, frequency response

analysis is conducted (i.e. without wear analysis) for the model with 20 friction elements with both numerical and analytical Jacobian calculation. Solution times for a standard laptop are compared in Table 5.6. It's demonstrated that analytical Jacobian requires 35 times less solution time when compared with the numerical one. This result shows that wear analysis with hundreds of friction elements might not even be possible if the Jacobian is calculated numerically.

Table 5.6 Solution Time Comparison of Jacobian Calculation

Jacobian Calculation	Solution Time (sec)
Analytical	33.8
Numerical	1163.1

After wear analysis, for the two extreme cases, i.e. with 20 and 266 friction elements, contact status at the interface, which gives information about the dynamic behavior of the contact points, is shown in Figure 5.17. It can be seen that friction elements that lie away from the root of the blade deform more due to decreased stiffness of the geometry; hence, they are in fully stuck state.
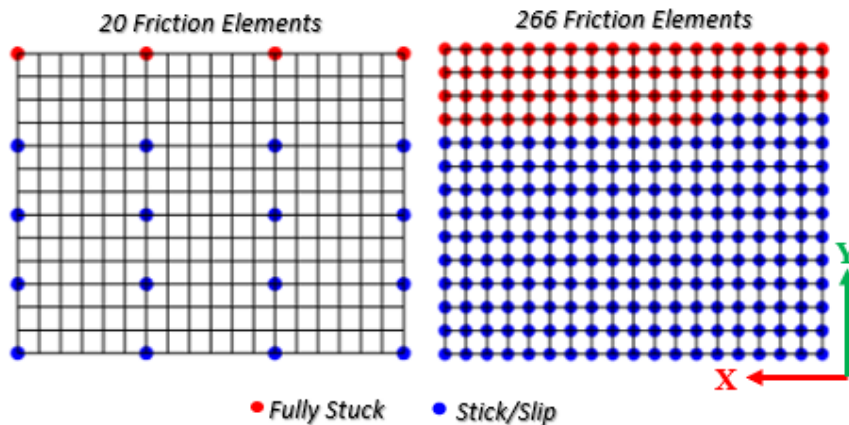

Figure 5.17 Contact Statuses for Unworn Structure

As explained before, the wear depth based algorithm requires δ_u for updating the nonlinear forced response analysis periodically and δ_{all} for finalizing the analysis. These parameters are taken as $\delta_u = 1\,\mu m$, $\delta_{all} = 60\,\mu m$ in this case study.

After the wear analysis, contact statuses of unworn structures have the same contact status at the same contact points which are given in Figure 5.18. Since nodes closer to the blade possess more slip behavior, the contact points at the lower part in Figure 5.18 experience separation in addition to stick and slip. This result becomes more meaningful when the wear map in Figure 5.19 is studied. It can be concluded from these results that contact status and wear depth at the local regions cannot be captured accurately if 20 friction elements are used compared to one with 266 friction elements.
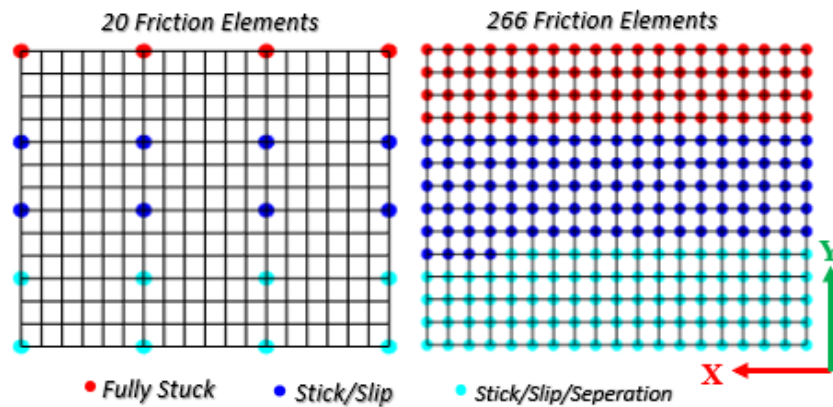

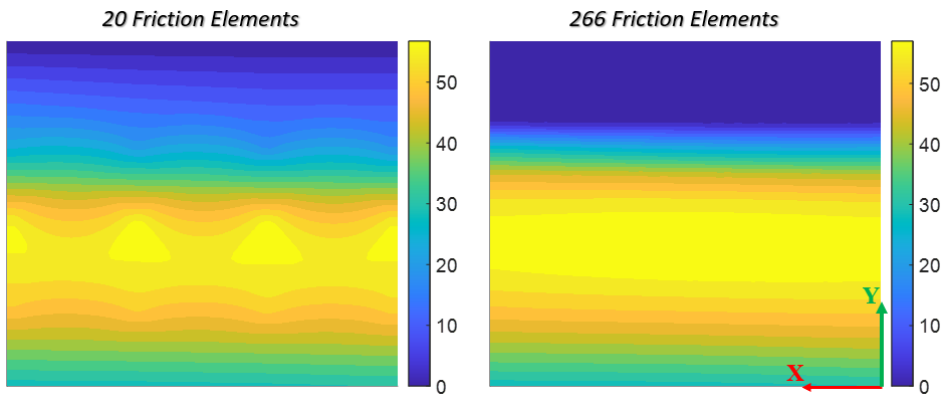Figure 5.18 Contact Statuses for Worn Structure

20 Friction Elements   266 Friction Elements

Figure 5.19 2D Wear Map $\left(\mu m\right)$

In Figure 5.20 and Figure 5.21 wear maps and difference in nodal wear depth are given in order to quantize and observe the effect of the number of contact nodes on the prediction of wear topography. It can be seen that more than $5\mu m$ of difference occurs in the common contact elements. Moreover, interpolated 3D wear maps are significantly different at certain local parts of the contact interface.
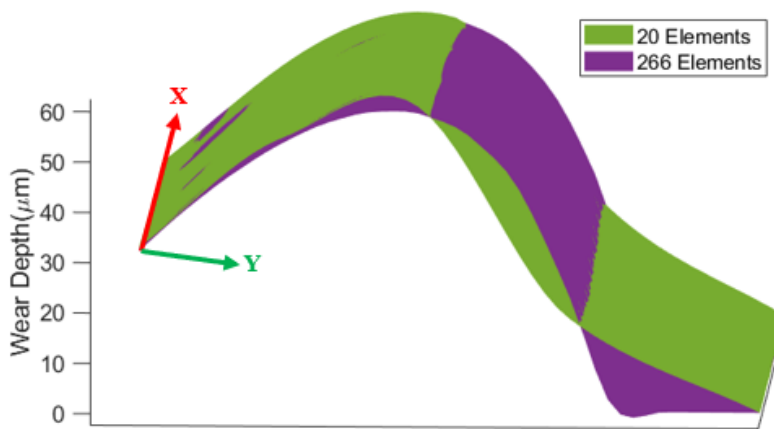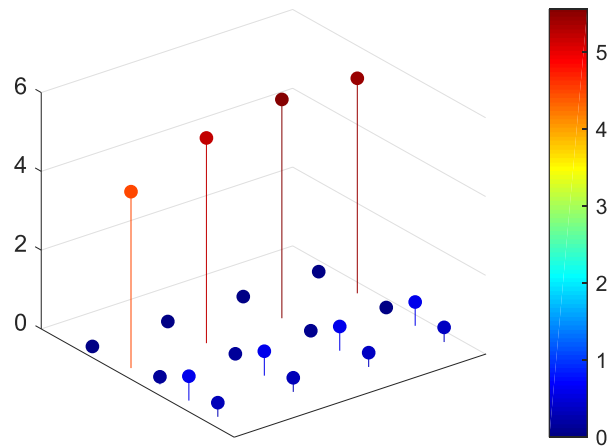

Figure 5.20 3D Wear Map Comparison $\left(\mu m\right)$

Figure 5.21 Difference in Nodal Wear Depth (μm)

However, on the other side, nonlinear responses of the blade at point A given in Figure 5.22 show similar behavior for the case with 20 and 266 friction elements. Thus, from the perspective of nonlinear forced response, both models give similar results due to the same allowable nodal wear depth inputs (δ_{all}) and relatively similar wear topographies.
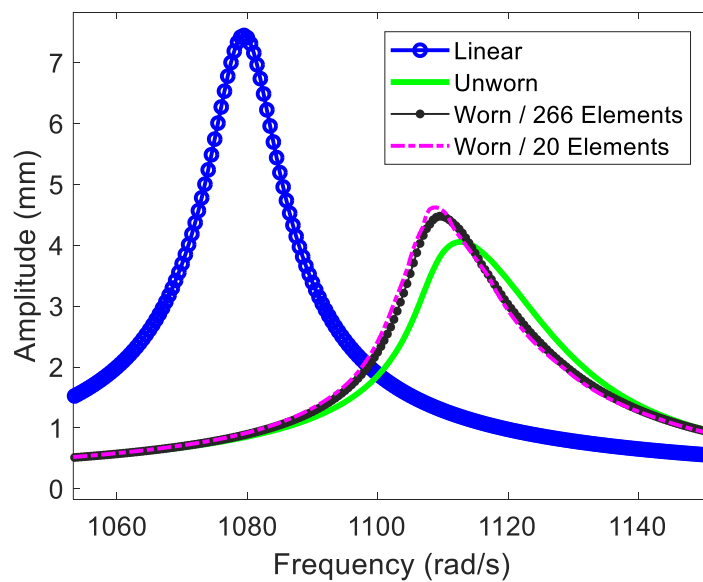

Figure 5.22 Frequency Response After Wear Analysis

From the predictive maintanance perspective, total working period of the friction damper can also be calculated. While 187.0 hours are required for the contact interface with 20 friction elements to reach the corresponding δ_{all}, the model with 266 friction elements results in 177.0 hours.

Although, this result clarifies that two extreme conditions, 266 and 20 friction elements, converge almost same frequency responses in a similar operation period, the trend while increasing number of friction elements used at the contact interface should be shought. For this purpose, contact elements are evenly distrubuted over the equally meshed contact interface with different numbered of friction elements as shown in Figure 5.23.
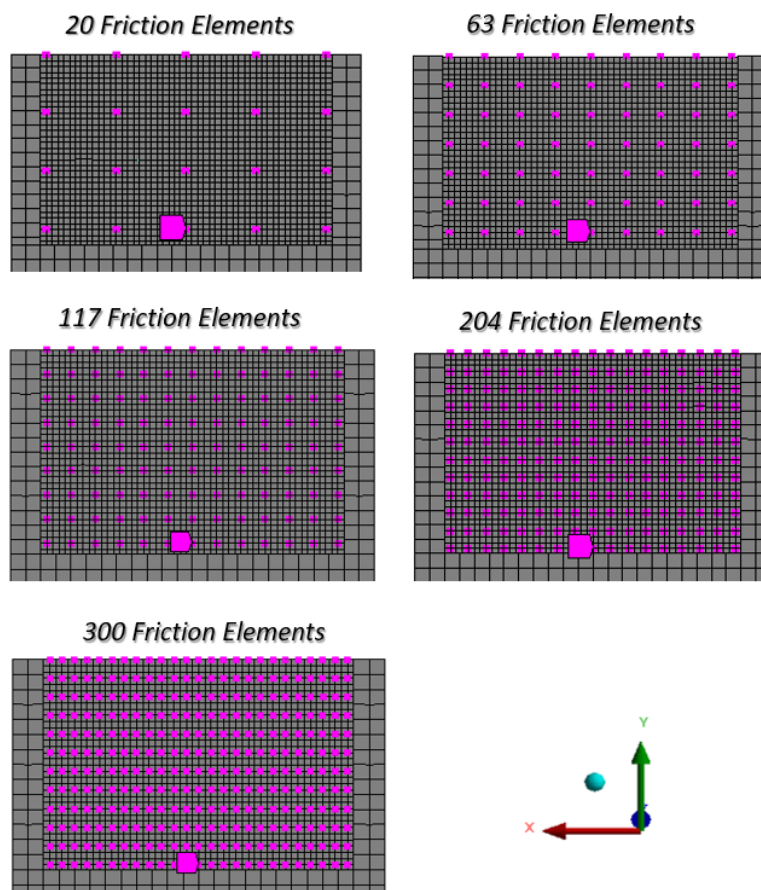

Figure 5.23 Distribution of Friction Elements on the Contact Patch

To verify the algorithm presented in Section 4.2, analysis is conducted with wear cycle based approach by taking $N_c = 5 \times 10^6$ and $N_{c_{all}} = 10^9$.

Note that operation time in hours $\left(t_h\right)$ can also be calculated from (4.15). For the operation frequency of $\omega_{op} = 1115 \, rad/s$ and total operation cycles of $N_{c_{all}} = 10^9$, t_h can be calculated as $249.1 \, hours$. Hence, following findings are the results of $249.1 \, hours$ of operation time.

After wear analysis, frequency responses are plotted in Figure 5.24. Although, responses give quite close results, the absolute errors need to be analyzed to investigate the trend while increasing number of friction elements used in the model.
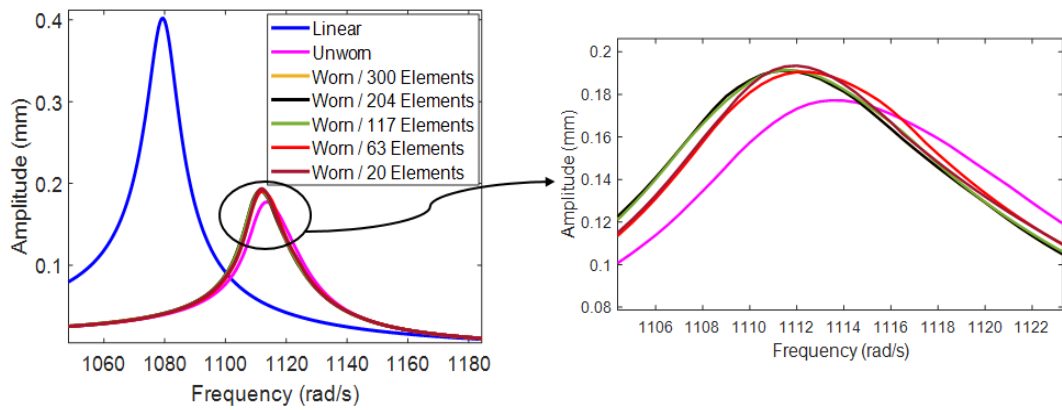

Figure 5.24 Frequency Response After Wear Analysis

Figure 5.25 shows the relative error in resonance amplitude and frequency as a function of number of friction elements used with respect to the case with 300

elements. As the number of contact points decreases, shift in resonance frequency and the corresponding resonance amplitude increase.
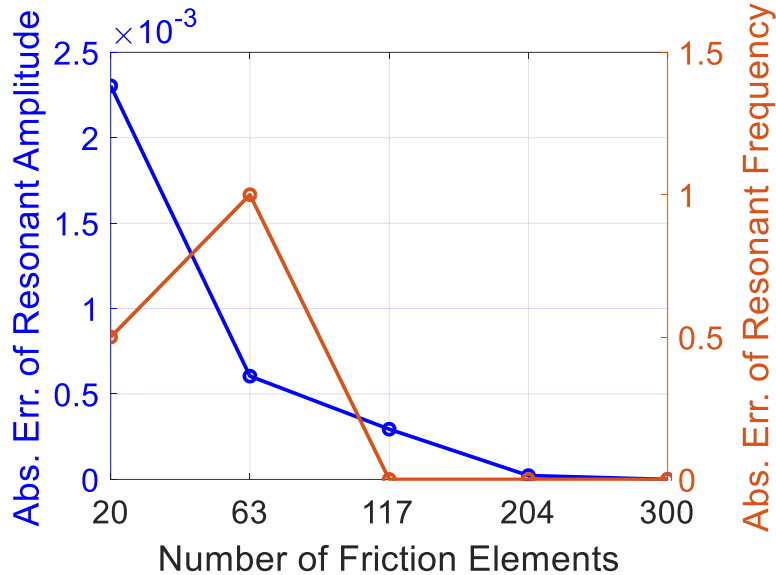

Figure 5.25 Absolute Error of Damped Resonant Amplitude and Frequency vs. Number of Friction Elements

In order to find a compromising contact element number for the analysis, percent errors shown in Figure 5.25 are compared with the solution time required. While the left y-axis of Figure 5.26 shows the percent error of the resonant amplitude, the right y-axis represents the normalized solution time. Computational time is normalized with respect to the results of the case with 20 friction elements. Note that the solution time required for the model with 20 friction elements is 13.1s on a standard laptop computer. It can be concluded that model with 204 elements can be a compromised model since the total solution time is about 2.5 times lower than the model with 300 friction elements as the percent amplitude error is at relatively low levels.
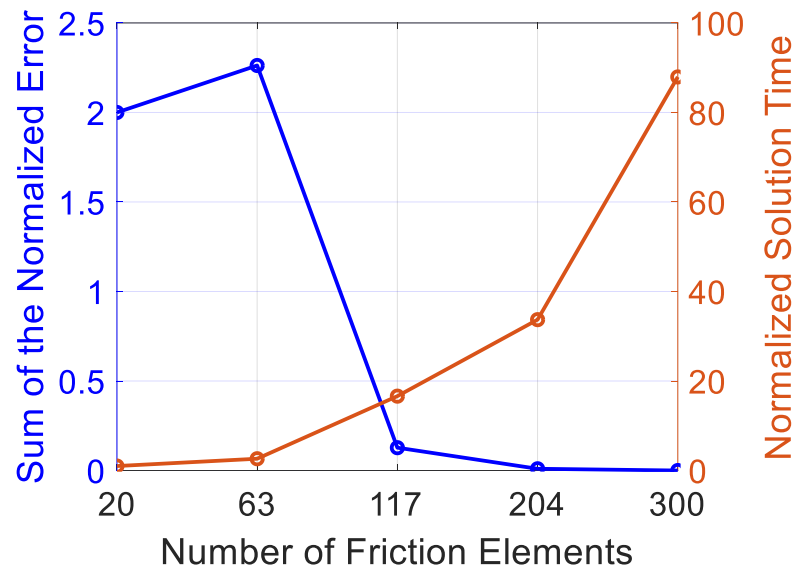
Figure 5.26 Absolute Percent Error of Damped Resonant Amplitude and
Normalized Solution Time vs. Number of Friction Elements

In this case study, the effect of the number of friction elements on fretting wear estimation and its effect on the nonlinear dynamic response is studied on a blade model with a platform damper with 20 and 266 contact points. Although the nonlinear forced responses show similar behavior for both cases, wear map has a notable difference at certain local areas where the model with less friction elements cannot capture the wear phenomenon accurately. Moreover, wear analysis is conducted with wear cycle based algorithm with various number of friction elements. It is observed that errors of resonant amplitude and resonant frequency has a decreasing trend while number of friction element used in the model increases.

CHAPTER 6

CONCLUSION

Dynamics of frictionally constraint structures have been deeply studied for over fifty years by scientists and engineers. One of the main examples of such structures is gas turbine engines in which friction is intentionally introduced which makes the problem highly nonlinear and unpredictable unless a sophisticated model is established. Hence, various friction models and solution methods are presented in the literature. To ensure the long-term performance of the design, fretting wear also needs to be included to the model so that catastrophic failures are avoided. However, fretting wear is either underestimated or studied superficially by not considering its complex nature.

In this thesis, during the ongoing friction cycles, the effect of fretting wear on the dynamic response, surface topology and deviation from the desired design region is studied by reducing solution time.

Before going deep into the fretting wear analysis, various contact models and fretting wear models are discussed. Along with 1D dry friction element with normal load variation and 3D dry friction element, analytical Jacobian formulations of these two contact models are presented which opens the way of faster computation.

As a next step, contact and fretting wear models are coupled. By this way, fretting wear is calculated at each contact node to feed its input to the contact model and find the frequency response of the worn profile at the intermediate steps during fretting cycles. Algorithms are established on two perspectives which are wear depth and wear cycle perspectives. While the wear depth perspective ends the algorithm when the maximum allowable wear depth is reached, the algorithm with wear cycle based perspective is run till the input total wear cycle (i.e. operation time).

To validate the proposed methodology, two numerical case studies are investigated. As a first case study, the shrouded blade is grounded. 3D dry friction element is used as a contact model. Wear depth based algorithm is employed to analyze the dynamic response at different wear depth values. Contact statuses at each intermediate wear depth values are also shown to understand how fretting wear causes shroud to be nonfunctional in a long run. Further, the effect of permissible wear depth which determines the update rate of wear calculation is also plotted and tabulated with respect to solution time. As a second case study, grounded blade platform is used to simplify the underplatform damper. In this study, 1D dry friction element is used and excitation force is exerted unidirectional. Different from the first case study, wear cycle based algorithm is also implemented to problem along with the wear depth based algorithm. By using these two fretting wear calculation perspectives, effect of wear on the dynamic response and contact topography transformation over ongoing friction cycle is discussed for various number of friction elements. It's shown that as number of friction element used in the model is increased, micro-level effects of wear become apparent and deficiency of macro-slip friction model is discovered.

As future work, proposed theoretical models, fretting wear analysis algorithms and numerical outputs of the case studies can be verified by a specially designed test rig and the results can be compared. Further, the microslip friction element can be employed as a contact model rather than the macroslip friction element which enables to capture the microslip effects of wear.

REFERENCES

[1] F. Marques, P. Flores, and H. M. Lankarani, "On the frictional contacts in multibody system dynamics," *Comput. Methods Appl. Sci.*, vol. 42, no. January, pp. 67–91, 2015, doi: 10.1007/978-3-319-30614-8_4.

[2] G. M. Jenkins, "Analysis of the stress-strain relationships in reactor grade graphite," *Br. J. Appl. Phys.*, vol. 13, no. 1, pp. 30–32, 1962

[3] A. Sinha and J. H. Griffin, "Friction damping of flutter in gas turbine engine airfoils," *J. Aircr.*, vol. 20, no. 4, pp. 372–376, 1983, doi: 10.2514/3.44878.

[4] E. H. Dowell and H. B. Schwartz, "Forced response of a cantilever beam with a dry friction damper attached, part I: Theory," *J. Sound Vib.*, vol. 91, no. 2, pp. 255–267, 1983, doi: 10.1016/0022-460X(83)90901-X.

[5] A. V. Srinivasan and D. G. Cutts, "Dry friction damping mechanisms in engine blades.," vol. 105, no. April 1983, 1982, doi: 10.1115/82-gt-162.

[6] C. H. Menq and J. H. Griffin, "A comparison of transient and steady state finite element analyses of the forced response of a friotionaily damped beam," *J. Vib. Acoust. Trans. ASME*, vol. 107, no. 1, pp. 19–25, 1985

[7] T. M. Cameron, J. H. Griffin, R. E. Kielb, and T. M. Hoosac, "An integrated approach for friction damper design," *J. Vib. Acoust. Trans. ASME*, vol. 112, no. 2, pp. 175–182, 1990, doi: 10.1115/1.2930110.

[8] J. H. Griffin and C. H. Menq, "Friction damping of circular motion and its implications to vibration control," *J. Vib. Acoust. Trans. ASME*, vol. 113, no. 2, pp. 225–229, 1991, doi: 10.1115/1.2930173.

[9] C. H. Menq, P. Chidamparam, and J. H. Griffin, "Friction damping of two-dimensional motion and its application in vibration control," *J. Sound Vib.*, vol. 144, no. 3, pp. 427–447, 1991, doi: 10.1016/0022-460X(91)90562-X.

[10] K. Y. Sanliturk and D. J. Ewins, "Modelling two-dimensional friction contact and its application using Harmonic balance method," *J. Sound Vib.*, vol. 193, no. 2, pp. 511–523, 1996, doi: 10.1006/jsvi.1996.0299.

[11] H. C. Menq, J. H. Griffin, and J. Bielak, "The influence of a variable normal load on the forced vibration of a frictionally damped structure.," vol. 108, no. April 1986, pp. 1–6, 1985.

[12] B. D. Yang and C. H. Menq, "Characterization of 3D contact kinematics and prediction of resonant response of structures having 3D frictional constraint," *J. Sound Vib.*, vol. 217, no. 5, pp. 909–925, 1998

[13]   B. D. Yang, M. L. Chu, and C. H. Menq, "Stick-slip-separation analysis and non-linear stiffness and damping characterization of friction contacts having variable normal load," *J. Sound Vib.*, vol. 210, no. 4, pp. 461–481, 1998, doi: 10.1006/jsvi.1997.1305.

[14]   T. M. Cameron, J. H. G. An, A. Frequency, and T. Domain, "An Alternating Frequency / Time Domain Method for Calculating the Steady-State Response of Nonlinear Dynamic Systems," 1989.

[15]   A. Cardona, T. Coune, A. Lerusse, and M. Geradin, "A multiharmonic method for non-linear vibration analysis," *Int. J. Numer. Methods Eng.*, vol. 37, no. 9, pp. 1593–1608, 1994, doi: 10.1002/nme.1620370911.

[16]   A. Cardona, A. Lerusse, and M. Géradin, "Fast Fourier nonlinear vibration analysis," *Comput. Mech.*, vol. 22, no. 2, pp. 128–142, 1998, doi: 10.1007/s004660050347.

[17]   W. Gu, Z. Xu, and S. Wang, "Advanced modelling of frictional contact in three-dimensional motion when analysing the forced response of a shrouded blade," *Proc. Inst. Mech. Eng. Part A J. Power Energy*, vol. 224, no. 4, pp. 573–582, 2010, doi: 10.1243/09576509JPE853.

[18]   D. Laxalde, F. Thouverez, J. J. Sinou, and J. P. Lombard, "Qualitative analysis of forced response of blisks with friction ring dampers," *Eur. J. Mech. A/Solids*, vol. 26, no. 4, pp. 676–687, 2007, doi: 10.1016/j.euromechsol.2006.10.002.

[19]   D. Laxalde and F. Thouverez, "Complex non-linear modal analysis for mechanical systems: Application to turbomachinery bladings with friction interfaces," *J. Sound Vib.*, vol. 322, no. 4–5, pp. 1009–1025, 2009, doi: 10.1016/j.jsv.2008.11.044.

[20]   C. M. Firrone and S. Zucca, "Modelling Friction Contacts in Structural Dynamics and its Application to Turbine Bladed Disks," 2009.

[21]   H. C. Meng and K. C. Ludema, "Wear models and predictive equations: their form and content," *Wear*, vol. 181–183, no. PART 2, pp. 443–457, 1995, doi: 10.1016/0043-1648(95)90158-2.

[22]   S. Montgomery, D. Kennedy, N. O 'dowd, S. J. Montgomery, and D. M. Kennedy, "Analysis of Wear Models for Advanced Coated Materials," pp. 0–16, 2009, [Online]. Available: http://arrow.dit.ie/engschmeccon.

[23]   J. F. Archard, "Contact and rubbing of flat surfaces," *J. Appl. Phys.*, vol. 24, no. 8, pp. 981–988, 1953, doi: 10.1063/1.1721448.

[24]   S. Fouvry, T. Liskiewicz, P. Kapsa, S. Hannel, and E. Sauger, "An energy description of wear mechanisms and its applications to oscillating sliding contacts," *Wear*, vol. 255, no. 1–6, pp. 287–298, 2003, doi: 10.1016/S0043-1648(03)00117-0.

[25] S. Fouvry, C. Paulin, and T. Liskiewicz, "Application of an energy wear approach to quantify fretting contact durability: Introduction of a wear energy capacity concept," *Tribol. Int.*, vol. 40, no. 10-12 SPEC. ISS., pp. 1428–1440, 2007, doi: 10.1016/j.triboint.2007.02.011.

[26] S. Fouvry, P. Duó, and P. Perruchaut, "A quantitative approach of Ti-6Al-4V fretting damage: Friction, wear and crack nucleation," *Wear*, vol. 257, no. 9–10, pp. 916–929, 2004, doi: 10.1016/j.wear.2004.05.011.

[27] R. Bassani and M. D. Acunto, "Nanotribology : tip – sample wear under adhesive contact," vol. 33, pp. 443–452, 2000.

[28] A. Zmitrowicz, "A thermodynamical model of contact, friction and wear: I governing equations," *Wear*, vol. 114, no. 2, pp. 135–168, 1987, doi: 10.1016/0043-1648(87)90086-X.

[29] D. Laxalde, L. Salles, L. Blanc, and F. Thouverez, "Non-linear modal analysis for bladed disks with friction contact interfaces," *Proc. ASME Turbo Expo*, vol. 5, no. PART A, pp. 457–467, 2008, doi: 10.1115/GT2008-50860.

[30] L. Salles, L. Blanc, F. Thouverez, and A. M. Gouskov, "Dynamic analysis of fretting-wear in friction contact interfaces," *Int. J. Solids Struct.*, vol. 48, no. 10, pp. 1513–1524, 2011, doi: 10.1016/j.ijsolstr.2011.01.035.

[31] J. Armand, L. Pesaresi, L. Salles, and C. W. Schwingshackl, "A Multiscale Approach for Nonlinear Dynamic Response Predictions with Fretting Wear," *J. Eng. Gas Turbines Power*, vol. 139, no. 2, 2016, doi: 10.1115/1.4034344.

[32] J. Armand, L. Pesaresi, L. Salles, C. Wong, and C. W. Schwingshackl, "A modelling approach for the nonlinear dynamics of assembled structures undergoing fretting wear," *Proc. R. Soc. A Math. Phys. Eng. Sci.*, vol. 475, no. 2223, 2019, doi: 10.1098/rspa.2018.0731.

[33] E. Lemoine, D. Nélias, F. Thouverez, and C. Vincent, "Influence of fretting wear on bladed disks dynamic analysis," *Tribol. Int.*, vol. 145, no. January, p. 106148, 2020, doi: 10.1016/j.triboint.2019.106148.

[34] L. R. Tamatam, D. Botto, and S. Zucca, "A coupled approach to model the effect of wear on the dynamics of bladed disks," *Proc. 26th Int. Congr. Sound Vib. ICSV 2019*, pp. 1–29, 2019.

[35] G. Von Groll and D. J. Ewins, "The harmonic balance method with arc-length continuation in rotor/stator contact problems," *J. Sound Vib.*, vol. 241, no. 2, pp. 223–233, 2001, doi: 10.1006/jsvi.2000.3298.

[36] Å. Kassman, S. Jacobson, L. Erickson, P. Hedenqvist, and M. Olsson, "A new test method for the intrinsic abrasion resistance of thin coatings," *Surf. Coatings Technol.*, vol. 50, no. 1, pp. 75–84, 1991